Exciton-Exciton Interactions in Van der Waals Heterobilayers

Alexander Steinhoff[1,2,*], Edith Wietek[3], Matthias Florian,[4] Tommy Schulz[1,2], Takashi Taniguchi,[5]
Kenji Watanabe[6], Shen Zhao[7], Alexander Högele[7,8], Frank Jahnke,[1,2] and Alexey Chernikov[3]

[1]*Institut für Theoretische Physik, Universität Bremen, 28334 Bremen, Germany*
[2]*Bremen Center for Computational Materials Science, Universität Bremen, 28334 Bremen, Germany*
[3]*Institute of Applied Physics and Würzburg-Dresden Cluster of Excellence ct.qmat,*
Technische Universität Dresden, 01062 Dresden, Germany
[4]*Department of Electrical Engineering and Computer Science, University of Michigan,*
Ann Arbor, Michigan 48109, USA
[5]*Research Center for Materials Nanoarchitectonics, National Institute for Materials Science,*
1-1 Namiki, Tsukuba 305-0044, Japan
[6]*Research Center for Electronic and Optical Materials, National Institute for Materials Science,*
1-1 Namiki, Tsukuba 305-0044, Japan
[7]*Fakultät für Physik, Munich Quantum Center, and Center for NanoScience (CeNS),*
Ludwig-Maximilians-Universität München, 80539 München, Germany
[8]*Munich Center for Quantum Science and Technology (MCQST), 80799 München, Germany*

Exciton-exciton interactions are key to understanding nonlinear optical and transport phenomena in van der Waals heterobilayers, which emerged as versatile platforms to study correlated electronic states. We present a combined theory-experiment study of excitonic many-body effects based on first-principle band structures and Coulomb interaction matrix elements. Key to our approach is the explicit treatment of the fermionic substructure of excitons and dynamical screening effects for density-induced energy renormalization and dissipation. We demonstrate that dipolar blueshifts are almost perfectly compensated by many-body effects, mainly by screening-induced self-energy corrections. Moreover, we identify a crossover between attractive and repulsive behavior at elevated exciton densities. Theoretical findings are supported by experimental studies of spectrally narrow, mobile interlayer excitons in atomically reconstructed, h-BN-encapsulated $MoSe_2$/WSe_2 heterobilayers. Both theory and experiment show energy renormalization on a scale of a few meV even for high injection densities in the vicinity of the Mott transition. Our results revise the established picture of dipolar repulsion dominating exciton-exciton interactions in van der Waals heterostructures and open up opportunities for their external design.

I. INTRODUCTION

Vertically stacked van der Waals heterobilayers with type-II band alignment host layer-separated, Coulomb-correlated electron-hole pairs forming interlayer excitons (ILXs) with binding energies of more than 100 meV and lifetimes that are often drastically increased in comparison to excitons within a single layer [1–7]. For a wide range of electron-hole densities below the excitonic Mott transition [8,9], ILXs constitute an interacting quantum gas with renormalized spectral properties. Exciton-exciton interactions are of major importance in the context of understanding on-site repulsion energies and emerging many-body states in moiré systems [10–14], excitonic transport [15–20], and nonlinear optical response [21–23]. Importantly, they lead to excitation-dependent shifts of the exciton resonance toward higher energies, in close analogy to the physics of coupled quantum well systems [24–29]. These energy shifts are broadly used as key observables to assess the strength of the exciton-exciton coupling and determine exciton densities [30,31].

Conventionally, the interaction is described in the semiclassical picture of long-range repulsion between two dipoles representing spatially indirect excitons [32,33]. Corresponding theoretical descriptions range from basic capacitor models [26,29] to correlation-corrected formulas [27,28], microscopic theories beyond the effective bosonic

picture [34,35], and adaptations of classical approaches to describe localized moiré excitons [36–38]. Nevertheless, the dominating picture of exciton-exciton interactions broadly used in the field of van der Waals heterostructures remains based on the dipole-dipole repulsion. Only recently, predictions of additional contributions emerged, associated with exchange interaction and Pauli blockade from the underlying fermionic substructure [18,39]. This state of affairs strongly suggests to test and revise the dipolar description of the exciton-exciton interaction in van der Waals heterostructures, motivating the development of a comprehensive theoretical approach and a well-defined experimental setting.

Here, we present a combined theory-experiment study of density-dependent exciton energy renormalizations based on a systematic many-body description of interacting excitons as composite particles. We determine both the resulting energy shifts and scattering-induced spectral broadening. Supported by spectroscopic measurements of mobile excitons in atomically reconstructed, h-BN-encapsulated $MoSe_2/WSe_2$ heterobilayers, we find that the classical dipolar description drastically overestimates the interaction strength. We show that the dipole-dipole repulsion is largely compensated by competing many-body effects within the dense exciton gas, including correction terms due to the fermionic substructure and screening. Several contributions have large absolute values yet opposite signs. As a net result, exciton energies shift by only a few meV even at exciton densities close to ionization threshold above 10^{12} cm^{-2}. Moreover, we demonstrate that the interplay of different renormalization effects can result in an effectively *attractive* interaction with a density-dependent crossover to the repulsive regime.

To obtain quantitative results, we consider a representative case of an H-stacked $MoSe_2/WSe_2$ heterobilayer encapsulated in hexagonal boron nitride (h-BN) and build on a theory for the dense exciton gas based on two-particle Green functions [34,40]. Key to our method development is the combination of this established many-body theory with material-realistic band structure and Coulomb matrix element calculations, augmented by frequency-dependent excitonic screening effects. The starting point of our calculations is the Bethe-Salpeter equation in the absence of photoexcited carriers:

$$(\varepsilon_{\mathbf{Q}-\mathbf{k}}^{e} + \varepsilon_{\mathbf{k}}^{h} - E_{\nu,\mathbf{Q}})\Phi_{\nu,\mathbf{Q}}(e, h, \mathbf{k})$$
$$- \sum_{\mathbf{q}, h', e'} V_{\mathbf{Q}-\mathbf{k},\mathbf{k},\mathbf{k}+\mathbf{q},\mathbf{Q}-\mathbf{k}-\mathbf{q}}^{e,h,h',e'} \Phi_{\nu,\mathbf{Q}}(e', h', \mathbf{k}+\mathbf{q}) = 0, \quad (1)$$

which we solve to obtain exciton wave functions $\Phi_{\nu,\mathbf{Q}}(e, h, \mathbf{k})$ and energies $E_{\nu,\mathbf{Q}}$. Here, exciton eigenstates are classified in terms of a quantum number ν for the relative electron-hole motion and the total exciton momentum $\mathbf{Q}$. First-principle band structures $\varepsilon_{\mathbf{k}}^{a}$ and dielectrically

screened Coulomb matrix elements $V_{\mathbf{k},\mathbf{k}',\mathbf{k}'+\mathbf{q},\mathbf{k}-\mathbf{q}}^{a,b,b',a'}$ are used in the electron-hole picture, expanding beyond the macroscopic Coulomb interaction model and parabolic bands employed in the literature [18]. In the exciton representation, we formulate a self-consistency equation for renormalized exciton energies as

$$\tilde{E}_{\nu,\mathbf{Q}} = E_{\nu,\mathbf{Q}} + \mathrm{Re}\Sigma(\nu, \mathbf{Q}, \tilde{E}_{\nu,\mathbf{Q}}/\hbar), \quad (2)$$

with the frequency-dependent exciton self-energy

$$\Sigma(\nu, \mathbf{Q}, \omega) = \Sigma^{\mathrm{H}}(\nu, \mathbf{Q}) + \Sigma^{\mathrm{F}}(\nu, \mathbf{Q}) + \Sigma^{\mathrm{PB}}(\nu, \mathbf{Q})$$
$$+ \Sigma^{\mathrm{MW, ret}}(\nu, \mathbf{Q}, \omega). \quad (3)$$

Explicit expressions as well as a detailed derivation of the various self-energy contributions are given in Appendix A. Energy renormalizations are accompanied by excitation-induced broadening determined by $\Gamma_{\nu,\mathbf{Q}} = -\mathrm{Im}\Sigma(\nu, \mathbf{Q}, \tilde{E}_{\nu,\mathbf{Q}})$, where $2\Gamma_{\nu,\mathbf{Q}}$ corresponds to the full width at half maximum (FWHM) of the homogeneous exciton linewidth. The self-energy consists of Hartree (H), Fock (F), Pauli blocking (PB), and Montroll-Ward (MW) terms. The different contributions to exciton-exciton interaction described by the exciton self-energy are schematically shown in Fig. 1. A part of the Hartree term represents classical electrostatic interaction between excitons [Fig. 1(a)]. It is of dipole-dipole type and contains two repulsive and two attractive contributions. Since like charges reside within the same layer in type-II heterobilayers, the repulsive terms dominate over the attractive interlayer terms. Therefore, the net effect is a pronounced blueshift of exciton energies. On the other hand, exchange interaction between the fermionic constituents of excitons [included in both Hartree and Fock terms, Fig. 1(b)] leads to an attractive interaction as in a Fermi gas. Excitons as composite bosons also experience a repulsive bosonic exchange interaction that is sketched in Fig. 1(c), represented by the Fock term in Eq. (3). This can be understood as the consequence of boson statistics favoring occupation of the same states that, in turn, leads to stronger Coulomb repulsion.

Pauli blocking of the fermionic phase space due to the exciton substructure is illustrated in Fig. 1(d). It acts as a source of the increased energy of the exciton transition, well known from the semiconductor Bloch equations [39,41,42]. Finally, the Montroll-Ward self-energy contains all noninstantaneous contributions of the GW self-energy, describing frequency-dependent screening of bosonic exchange interaction by excitations within the dense exciton gas. As discussed further below, this is a particularly important contribution to density-dependent exciton energy renormalizations that is explicitly treated beyond a more phenomenological description of static excitonic screening in the literature [18]. The result is a decrease of the exciton
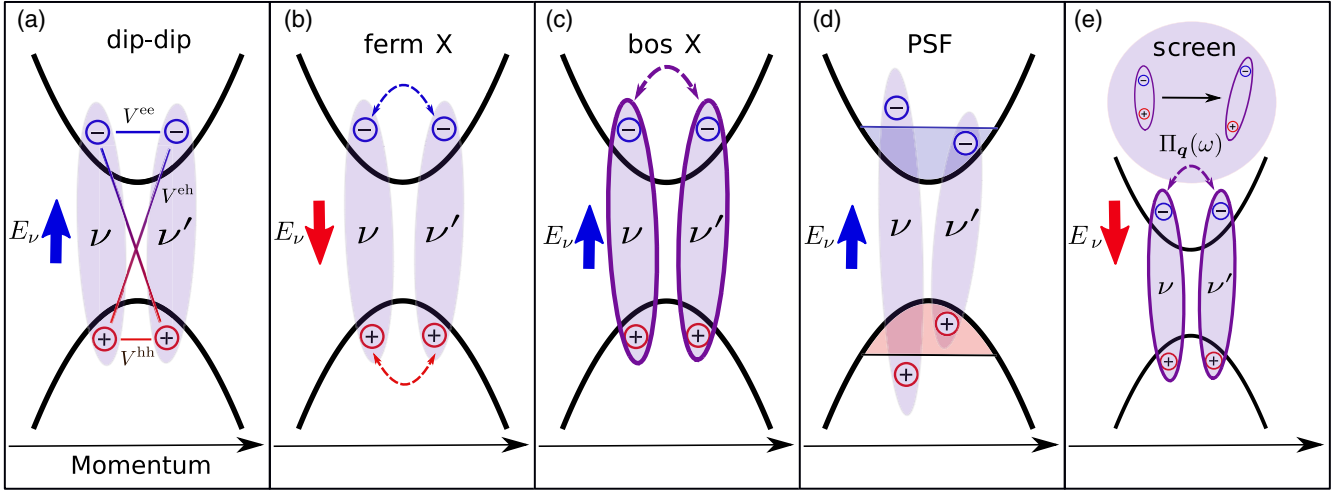
FIG. 1.   Contributions to exciton-exciton interaction. (a) Dipole-dipole interaction (dip-dip) between excitons in states ν and ν'. The process is composed of elementary Coulomb interaction between the electron of ν and the electron of ν', proportional to the matrix element V^{ee}, and between the electron of ν and the hole of ν' (V^{hh}) as well as corresponding electron-hole terms (V^{eh}). The resulting shift of the exciton energy E_ν is positive. (b) Fermionic exchange interaction (ferm X) between electrons or holes that are part of two different excitons, resulting in a decrease of the exciton energy. (c) Bosonic exchange interaction (bos X) of the whole excitons, resulting in an increase of the exciton energy. (d) Phase-space filling (PSF) due to fermionic constituents of exciton ν' as experienced by exciton ν, which yields an increase of E_ν. (e) Screened bosonic exchange interaction (screen) from the exciton Montroll-Ward (MW) self-energy. The interaction process is screened by a momentum- and frequency-dependent excitonic polarization $\Pi_{\mathbf{q}}(\omega)$ corresponding to scattering processes of surrounding excitons between different internal states, which results in a lowering of exciton energy.

energies, conceptually similar to the excitation-induced band gap renormalization [41–44].

II. EXPERIMENTAL SETUP

The experiments are performed on a $MoSe_2/WSe_2$ heterobilayer encapsulated in high-quality h-BN. We employ fabrication conditions of near-sixty-degree stacking favoring large-scale atomic reconstruction [45], thus suppressing formation of moiré patterns to achieve a flat potential landscape. The H_h^h registry is identified by its characteristic photoluminescence (PL) signatures, optical selection rules, and associated g factors [20]. The PL spectra feature low-energy triplet- and high-energy singlet-spin configurations with narrow linewidths of the exciton resonances down to a few meV confirming the sample quality. As localization of ILXs is suppressed in H_h^h reconstructed samples, the excitons are mobile, exhibiting phonon-limited free diffusion at lowest temperatures. This is particularly important, since the residual linewidth is likely to be determined by small inhomogeneous broadening in addition to phonon-induced scattering. Experimental demonstration of free exciton diffusion at 5 K in this type of h-BN-encapsulated monolayers [46] and heterobilayers [20] shows that the remaining potential fluctuations occur on comparatively large spatial scales. We, thus, stress the absence of evidence for exciton localization in the studied sample to compare the obtained results with theoretical calculations based on the assumption of spatially flat potentials. Furthermore, signatures of exciton-exciton annihilation and repulsion

validate that the excitons can scatter and interact efficiently with each other [20].

The measurements are performed in an optical microscopy cryostat at the temperatures of 5 and 70 K. The sample is excited by a pulsed, 140 fs Ti:sapphire laser with a repetition rate of 80 MHz and its excitation wavelength tuned resonantly into the $A\!:\!1s$ state of $MoSe_2$. The excitation energy densities ranged from 0.2 to 20 μJ/cm² per pulse. Assuming an absorbance of 11%, as estimated from reflectance measurements, we determine the corresponding peak exciton densities of 6×10^{10} and 6×10^{12} cm⁻² (see Appendix B for details). The PL is spectrally dispersed by a spectrometer and detected by a streak camera and a charge-coupled device for time-resolved and time-integrated measurements, respectively.

III. RESULTS

To quantify many-body renormalizations due to the exciton-exciton interaction, we solve Eq. (2) self-consistently for various exciton temperatures and densities. The static renormalizations contained in the self-energy (3) are explicitly given by

$$\Sigma^{\text{H}}(\nu, \mathbf{Q}) = \sum_{\nu', \mathbf{Q}'} \left(\tilde{V}_{\mathbf{Q}, \mathbf{Q}', \mathbf{Q}', \mathbf{Q}}^{(\text{D}), \nu, \nu', \nu', \nu} - \tilde{V}_{\mathbf{Q}, \mathbf{Q}', \mathbf{Q}', \mathbf{Q}}^{(\text{X}), \nu, \nu', \nu', \nu} \right) N_{\nu', \mathbf{Q}'}^{\text{X}}, \quad (4)$$

$$\Sigma^{\text{F}}(\nu, \mathbf{Q}) = \sum_{\nu', \mathbf{Q}'} \left(\tilde{V}_{\mathbf{Q}, \mathbf{Q}', \mathbf{Q}, \mathbf{Q}'}^{(\text{D}), \nu, \nu', \nu, \nu'} - \tilde{V}_{\mathbf{Q}, \mathbf{Q}', \mathbf{Q}, \mathbf{Q}'}^{(\text{X}), \nu, \nu', \nu, \nu'} \right) N_{\nu', \mathbf{Q}'}^{\text{X}}, \quad (5)$$
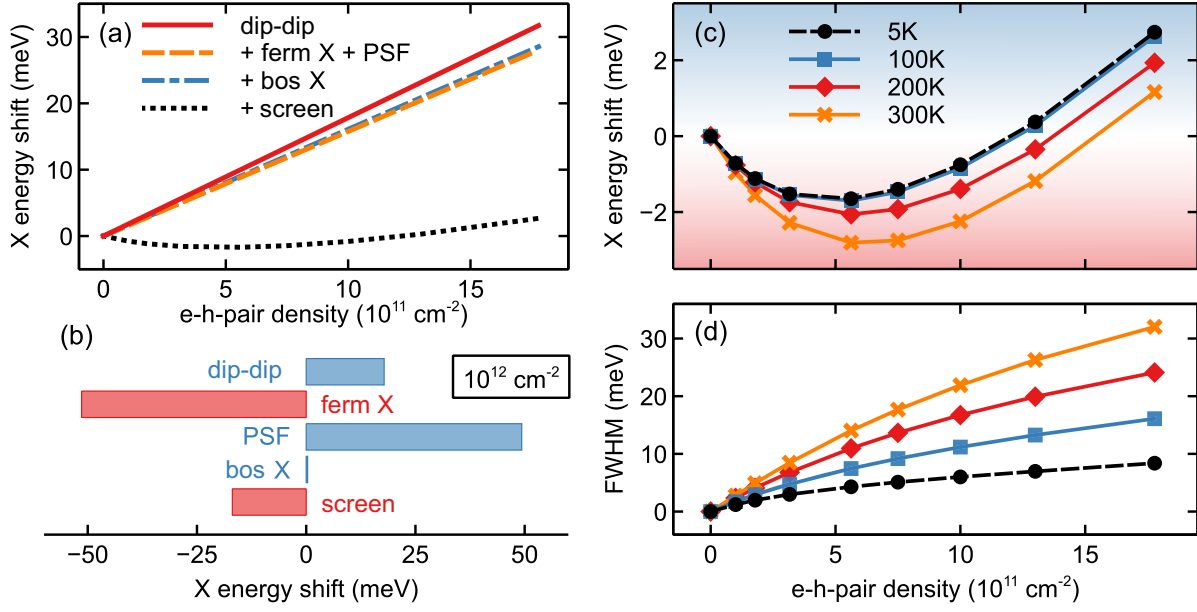
FIG. 2. Exciton energy renormalization induced by exciton-exciton interaction. (a) Cumulative density-dependent renormalization of the zero-momentum bright $1s$-exciton (spin-singlet) energy at a temperature $T = 100$ K, subsequently adding dipole-dipole interaction (dip-dip), fermionic exchange interaction and phase-space filling (+ ferm X + PSF), bosonic exchange interaction (+ bos X), and screened bosonic exchange (+ screen). The latter represents the result of the full calculation. (b) Individual contributions to the exciton energy renormalization corresponding to the cumulative presentation in (a) at an electron-hole pair density of 10^{12} cm^{-2}. The redshift due to fermionic exchange and the blueshift due to phase-space filling compensate to a large extent. (c) Calculated temperature and density dependence of energy renormalization for the zero-momentum bright $1s$ exciton. The result for $T = 5$ K has been obtained from extrapolating the high-temperature data. (d) Calculated temperature and density dependence of the zero-momentum bright $1s$-exciton broadening.

$$\Sigma^{\text{PB}}(\nu, \mathbf{Q}) = \sum_{\nu', \mathbf{Q}'} \left(\tilde{V}^{\text{PB},\nu,\nu',\nu',\nu}_{\mathbf{Q},\mathbf{Q}',\mathbf{Q}',\mathbf{Q}} + \tilde{V}^{\text{PB},\nu,\nu',\nu,\nu'}_{\mathbf{Q},\mathbf{Q}',\mathbf{Q},\mathbf{Q}'} \right) N^{\text{X}}_{\nu',\mathbf{Q}'}, \quad (6)$$

with effective exciton-exciton interaction matrix elements $\tilde{V}$ as defined in Appendix A and exciton populations $N^{\text{X}}_{\nu,\mathbf{Q}}$. Dielectric screening by the h-BN environment is modeled by an effectively isotropic dielectric constant $\varepsilon_{h\text{-BN}} = \sqrt{4.95 \times 2.86} \approx 3.76$ [47]. We consider the interlayer excitons populating the K and K' valleys of the two lowest conduction and two highest valence bands, respectively. The focus on K-valley states is motivated by their representative nature for interlayer excitons and by the absence of signatures from momentum-indirect excitons in the experiment [20]. For the bright spin-singlet states, we obtain a binding energy of 131 meV in good agreement with typical experimental values [4]. Finally, we limit the exciton density range to be below the predicted exciton Mott density $n_{\text{Mott}} \approx 2 \times 10^{12}$ cm^{-2} for this material system [20].

Numerical results of our calculations are shown in Fig. 2. In Fig. 2(a), we analyze the cumulative effect of all contributions to exciton-exciton interaction that have been introduced in Fig. 1 for the $1s$ exciton with vanishing total momentum $\mathbf{Q} = 0$ and bright spin-singlet configuration. The individual contributions are presented in Fig. 2(b).

The repulsive dipole-dipole interaction given by the exciton Hartree self-energy without fermionic correction terms [first term in Eq. (4)] yields a linear blueshift of up to 30 meV at the highest density close to 2×10^{12} cm^{-2}. The blueshift is reduced by the combination of fermionic exchange contributions, which are part of Hartree and Fock self-energies [second terms in Eqs. (4) and (5)], respectively, and Pauli blocking. The latter originates from the filling of phase space by the fermionic constituents of excitons, as described by the self-energy in Eq. (6). Fermionic exchange and Pauli blocking, although on the order of 50 meV each at a density of 10^{12} cm^{-2}, compensate each other to a large extent.

Bosonic exchange of excitons as described by the Fock self-energy without fermionic terms [first term in Eq. (5)] yields only a weak additional blueshift on the few-meV scale. The relative weakness compared to the direct exciton-exciton interaction can be partly understood from the dependence of the different self-energies on exciton populations. While the Hartree-like renormalization of a certain exciton state is approximately proportional to the total exciton density, $\Sigma^{\text{H},(\text{D})}(\nu, \mathbf{Q}) \approx \tilde{V}^{(\text{D})}_{\mathbf{Q}=0} \sum_{\nu', \mathbf{Q}'} N^{\text{X}}_{\nu',\mathbf{Q}'}$, the Fock-like term has a strong dependence on the momentum and spin distribution of excitons, $\Sigma^{\text{F},(\text{D})}(\nu, \mathbf{Q}) \approx \sum_{\nu', \mathbf{Q}'} \tilde{V}^{(\text{D})}_{|\mathbf{Q}-\mathbf{Q}'|} \delta_{s_e(\nu),s_e(\nu')} \delta_{s_h(\nu),s_h(\nu')} N^{\text{X}}_{\nu',\mathbf{Q}'}$.

Thus, bosonic exchange is sensitive only to a fraction of the total exciton density, which splits into intra- and intervalley excitons with like and unlike electron (s_e) and hole spins (s_h).

Finally, dynamical screening of the Coulomb interaction due to the presence of a polarizable exciton gas provides a substantial contribution to the energy renormalization. It is represented by the Montroll-Ward self-energy (A71), which contains the noninstantaneous contributions to the exciton GW self-energy, leading to a redshift on the order of tens of meV. Because of a sublinear increase of the redshift with the density, the cumulative energy renormalization is nonmonotonic. Although this self-energy is determined by frequency-dependent screening caused by the polarization of the dense exciton gas, we can understand its attractive character in the static limit (A80). Here, the self-energy splits into a contribution that leads to static screening of exciton exchange (without fermionic corrections) and a Coulomb hole (CH) contribution. The former yields a reduction of the weak momentum-dependent blueshift discussed above, while the latter is essentially a rigid redshift of the exciton dispersion. Since the CH shift is the dominant contribution, the Montroll-Ward self-energy is more sensitive to the total exciton density than to the distribution of excitons over the states.

To summarize these results in Figs. 2(a) and 2(b), the main competition takes place between the blueshift due to dipolar interaction and the redshift induced by excitonic screening, which are both sensitive to the total exciton density. This leads to the conclusion that the details of the exciton band structure are likely to be secondary for the total exciton shift. All in all, we find a remarkably strong compensation of different renormalization effects, leaving a net exciton blueshift of only a few meV even at high densities, close to the Mott transition. This density-dependent behavior is consistently found at both low and high temperatures, as shown in Fig. 2(c) for spin-bright excitons. For all temperatures, we find a few-meV redshift at small and intermediate densities which turns into a few-meV blueshift at high densities. This corresponds to a density-dependent crossover from an effectively attractive to repulsive exciton-exciton interaction. With decreasing temperature, the attractive character of interaction becomes slightly weaker yet also closer to the thermal energies of the excitons. Moreover, we confirm that similar behavior is expected for "gray" (spin-triplet) interlayer excitons, presented in Fig. 6 in Appendix A. Since the triplet exciton state is about 20 meV below the bright one, it is more strongly populated, which leads to an increase of fermionic and bosonic exchange effects among exciton triplets. As a result, the bright exciton interaction is slightly more repulsive.

Importantly, the noninstantaneous nature of the Montroll-Ward self-energy also results in a lifetime broadening of excitonic resonances according to Eq. (A79).

Temperature- and density-dependent results are shown in Fig. 2(d). Overall, we find a sublinear increase of broadening with the exciton density that is more pronounced at higher temperatures. At $T = 5$ K, we find a FWHM broadening of about 8 meV at highest densities, slightly larger than the typical linewidths of the exciton resonances in these systems, likely dominated by residual inhomogeneities. At elevated temperatures and densities, however, exciton-exciton scattering causes an increase of exciton linewidths by tens of meV, which is comparable to phonon-induced broadening [48–52]. Exciton-exciton scattering can, thus, provide a substantial contribution to dissipation and dephasing.

We also note that exciton-exciton annihilation [53–55] should not strongly contribute to the renormalization of the exciton energies. The associated changes of the exciton lifetimes are in the range of tens to hundreds of picoseconds for both as-exfoliated and h-BN-encapsulated samples [56]. The determined exciton-exciton annihilation coefficient is 5×10^{-3} cm^2/s in the studied MoSe$_2$/WSe$_2$ heterobilayer, corresponding to recombination rates below 0.1 ps^{-1} across the density range. The corresponding energy values are, thus, below 0.1 meV, justifying our theoretical approach that does not include this effect.

Theoretical results are confirmed by experimental observations presented in Fig. 3. As outlined in Sec. II, we ensure the following conditions for the experiment-theory comparison: suppression of long-range disorder [57], absence of moiré-like potentials from large-area atomic reconstruction [45], and the presence of mobile excitons even at low excitation densities [20]. All three conditions are important to avoid density-induced filling of localized tail states and demonstrate that the excitons can diffuse sufficiently far to interact with each other. The latter is particularly important and is the main reason for using the same sample as studied in Ref. [20] to extract density-dependent energy shifts. In the studied case, the excitons are shown to be mobile as well as subject to exciton-exciton repulsion and exciton-exciton annihilation, confirming the above.

A selection of time-integrated PL spectra for different exciton peak densities at a temperature of 5 K is shown in Fig. 3(a). The narrow linewidths allow for the distinct assignment of the PL peaks of charged (IX$_T^-$) and neutral (IX$_T^0$) interlayer triplets of H_h^h registry [20,45]. A small blueshift of only a few meV is observed for both exciton species up to highest densities in the range of the Mott transition, consistent with the literature for samples with sufficiently narrow linewidths [58]. Simultaneously, the relative PL weight shifts from IX$_T^-$ to IX$_T^0$ with increasing density. We note that, for sufficiently large spectral broadening, this shift of the center of gravity would lead to the appearance of a much larger blueshift. To illustrate that, the spectra are convoluted with a Gaussian (full width at half maximum of 15 meV), so that the PL of charged and
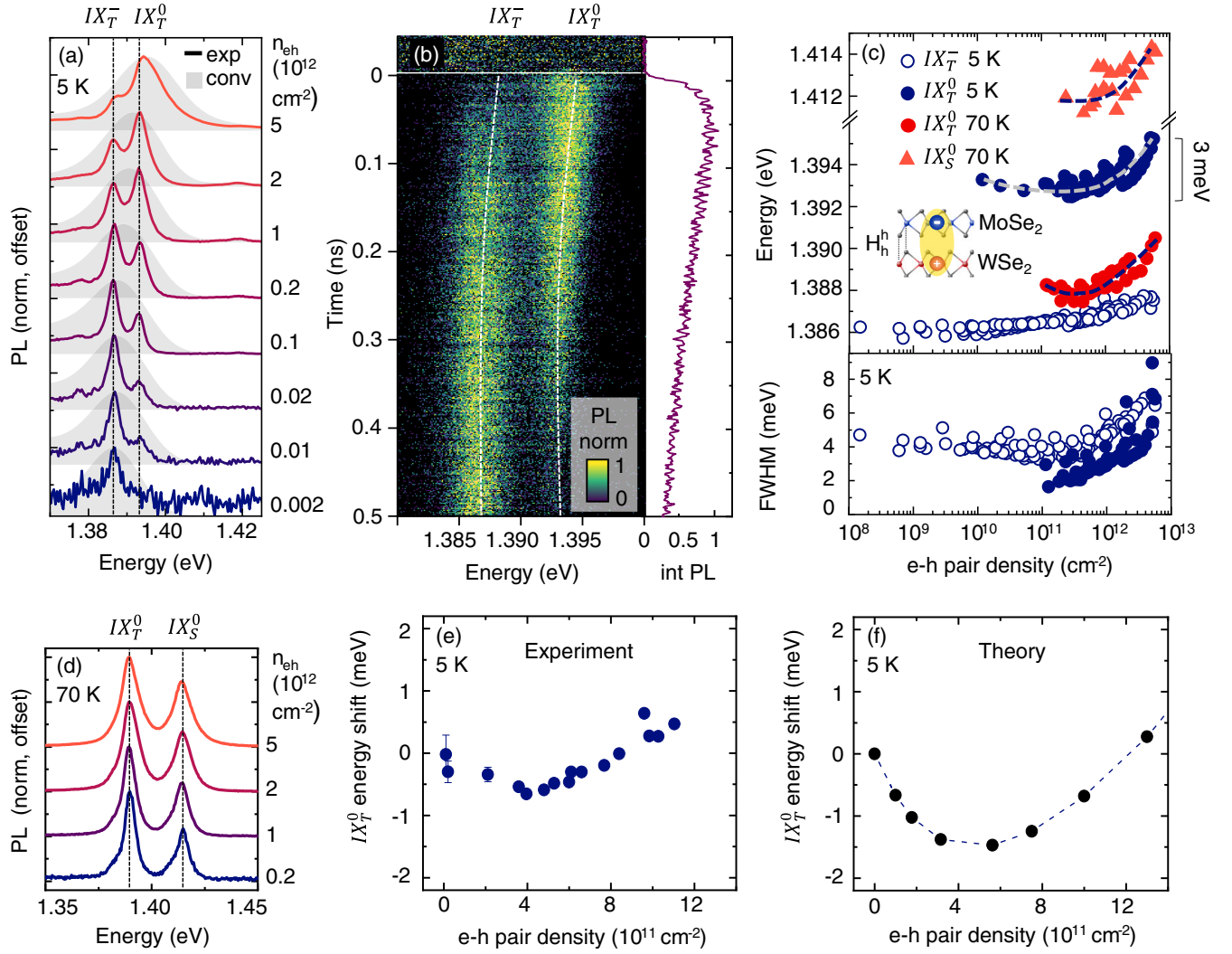
FIG. 3. Experimental energy shifts of interlayer excitons. (a) Time integrated spectra of K-K' interlayer excitons in an H_h^h reconstructed MoSe$_2$/WSe$_2$ heterobilayer for different exciton peak densities after pulsed excitation resonant with the MoSe$_2$ intralayer resonance at the lattice temperature of 5 K. For comparison, spectra convoluted with a Gaussian (FWHM of 15 meV) are presented to simulate additional inhomogeneous broadening. (b) Streak camera image of the spectrally and time-resolved PL at a peak density of 10^{12} cm^{-2}. The spectra are normalized at each time step, and the color scale is logarithmic. White dashed lines are guides to the eye, following the shift of the peak energy with time. Corresponding PL transient is presented in the right. (c) (Upper) Density-dependent energy shift of the interlayer exciton PL peaks at two different temperatures, extracted from time-resolved data. The resonances are labeled according to the previously identified excitons in the H_h^h-reconstructed MoSe$_2$/WSe$_2$ heterobilayer: charged and neutral interlayer triplets (IX$_T^0$ and IX$_T^-$) and the neutral interlayer singlet (IX$_S^0$). Dashed lines are guides to the eye. (Lower) Corresponding density-dependent linewidths of charged and neutral interlayer triplets at $T = 5$ K. The error bars for the extracted peak energies are below 1 meV for each individual data point, and there is a spread of the measured values from the two different analysis schemes and measurement series. (d) Selected PL spectra of neutral interlayer triplets and singlets at 70 K. (e) Extracted energy shifts of neutral interlayer triplets from experiment at 5 K. (f) Corresponding results from the calculations.

neutral excitons merges into one peak. By concealing the multipeak structure of the emission, the density-dependent blueshift is overestimated in contrast to weak shifts obtained for the individual peaks.

In addition to analyzing time-integrated spectra, we use an alternative method of investigating the effect of density on ILX via time-resolved PL. Taking advantage of the exciton decay, we relate the time axis to the relative change in exciton density, gaining access to quasi-instantaneous measurements of the energy shift at a given density. The exciton lifetimes on the order of hundreds of picoseconds are substantially longer than relevant timescales of the theoretically calculated phenomena. A representative time-resolved PL evolution at a nominal temperature of 5 K and peak electron-hole pair density of 10^{12} cm^{-2} is shown in Fig. 3(b). At time $t = 0$, the injected electron-hole pair

density is set equal to the estimated peak density. Consequently, at later times, the exciton density decreases proportionally to the decaying PL intensity, allowing us to extract the time-dependent peak position effectively as a function of density. This is reflected in the shift of the peak positions toward lower energies with time, as indicated by the dashed lines in Fig. 3(b). We evaluate the energy peak position for time steps of 50 ps width and assign the corresponding densities to values given by the injected maximum density and the relative change of PL intensity.

The results of both time-integrated and time-resolved analysis are summarized in Fig. 3(c), upper, for all measured triplet and singlet interlayer exciton states. The density range covers the linear regime up to the estimated Mott threshold of several 10^{12} cm^{-2} [9] and beyond. We note, however, that the main focus for the experiment-theory comparison is the low-to-intermediate regime of interacting, bound excitons below the Mott transition. The experiments are performed at a temperature of 5 K, to take advantage of the narrow linewidths and maximum PL yield, and at 70 K, where the influence of the interlayer trion in PL is negligible. Representative PL spectra of neutral interlayer triplets and singlets at 70 K are presented in Fig. 3(d). The maximum blueshift is found to be less or equal to 3 meV for all studied exciton species in good agreement with theory with weak indications of a redshift. A direct comparison between experiment and theory is presented in Figs. 3(e) and 3(f) for the case of the neutral interlayer triplets at 5 K. While there are quantitative differences between the curves, the overall behavior is very similar. Most importantly, the experiment does not show large shifts that would be otherwise expected from the simplified dipolar capacitor model.

The energy shifts are accompanied by a small spectral broadening at higher densities, similar to theoretically predicted values, as illustrated in Fig. 3(c), lower. We also note that the above observations are typical for samples with sufficiently narrow linewidths, as shown in Supplemental Material [59]. Also, the obtained data are subject to experimental error resulting in the spread of the measured values. Nevertheless, the experiments consistently reveal small energy shifts in the meV range, independent of the presence of charged excitons, observed at both low and elevated temperatures.

IV. CONCLUSIONS

In conclusion, we have demonstrated that the established picture of dipolar repulsion of interlayer excitons is insufficient and severely overestimates energy shifts resulting from exciton-exciton interaction. Among relevant contributions, we identify fermionic and bosonic exchange effects as well as the phase-space filling and excitonic screening that lead to renormalizations of comparable magnitude but opposite signs. The main competition takes place between the repulsive dipolar interaction and the attractive screening-induced self-energy correction, which both essentially depend on the total exciton density. The net result is an energy shift of only a few meV at exciton densities up to the Mott transition. Moreover, we demonstrate conditions for the emergence of weakly attractive exciton potentials, predicted to occur at low and intermediate densities. Interestingly, elevated temperatures yield a stronger tendency toward the attractive regime. In addition, the energy shifts are accompanied by scattering-induced spectral broadening of exciton states with a linear temperature dependence. The theoretical predictions are confirmed in experiment by taking advantage of well-defined, atomically reconstructed $MoSe_2/WSe_2$ heterobilayers void of localization with spectrally narrow resonances and mobile excitons. The magnitude of the measured energy shifts agrees with the results of the theoretical calculations within the experimental uncertainty. This holds both for low and elevated temperatures and is independent of the presence or absence of residual doping.

The developed understanding of the excitonic interactions has wide implications for the interpretation of optical and nonlinear transport phenomena as well as the overall phase diagram of interlayer excitons. It challenges the common notion of dominant dipole-dipole repulsion and offers a more nuanced approach to understanding exciton-exciton interactions in van der Waals heterostructures. Rendering the extraction of interlayer exciton densities from the energy shifts via capacitor model less useful than previously assumed, it highlights the importance of spectral analysis for samples featuring multiple, closely spaced resonances. Interestingly, one can expect that individual contributions to the exciton energy renormalization could be tunable using distinct sample geometries, dielectric environments, and external fields. Making use of this tunability, it should even be possible to design and switch between effectively repulsive and attractive interaction regimes. The implications range from the possible realization of local compression and excitonic droplets, to potentially favorable conditions for the formation of macroscopic many-body states such as superfluids and condensates. Natural extensions of the presented approach and results toward interlayer excitons in moiré and moiré-like superlattices would have major consequences for the on-site interaction terms determining the correlations. Overall, exciton-exciton interactions beyond the dipolar regime should have a substantial impact on the behavior of dense excitonic quantum gases on a fundamental level and be highly relevant for exploiting nonlinearities in photonic and optoelectronic applications.

APPENDIX A: THEORY

To obtain a material-realistic description of renormalization effects induced by exciton-exciton interactions, we combine first-principle band structures and Coulomb interaction matrix elements with a many-body theory for the dense exciton gas based on nonequilibrium Green functions. We essentially follow the derivation given by May, Boldt, and Henneberger [34,40], extending it with respect to (i) the generality of matrix elements and (ii) the inclusion of frequency-dependent screening effects.

1. Density functional theory calculations, spin-orbit coupling, and Coulomb matrix elements

Density functional theory (DFT) calculations for a freestanding H_h^h MoSe$_2$/WSe$_2$ heterobilayer are carried out using QUANTUM ESPRESSO V.6.6 [60,61]. We apply the generalized gradient approximation by Perdew, Burke, and Ernzerhof [62] and use an optimized norm-conserving Vanderbilt pseudopotential [63] at a plane-wave cutoff of 80 Ry. Uniform meshes (including the Γ point) with $18 \times 18 \times 1$ k points are combined with a Fermi-Dirac

smearing of 5 mRy. Using a fixed lattice constant of $a = 3.29$ Å [64] and a fixed cell height of 35 Å, forces are minimized below 5×10^{-3} eV/Å. The D3 Grimme method [65] is used to include van der Waals corrections.

We use RESPACK [66] to construct a lattice Hamiltonian $H_0(\mathbf{k})$ in a 22-dimensional localized basis of Wannier orbitals (d_{z^2}, d_{xz}, d_{yz}, $d_{x^2-y^2}$, and d_{xy} for Mo and W, respectively, and p$_x$, p$_y$, and p$_z$ for Se) from the DFT results. We also calculate the dielectric function as well as bare and screened Coulomb matrix elements in the localized basis. Spin-orbit interaction is included using an on-site $\boldsymbol{L} \cdot \boldsymbol{S}$-coupling Hamiltonian, which is added to the nonrelativistic Wannier Hamiltonian:

$$H(\mathbf{k}) = I_2 \otimes H_0(\mathbf{k}) + H_{\text{SOC}}. \tag{A1}$$

Here, I_2 is the 2×2 identity matrix in the Hilbert space spanned by eigenstates $|\uparrow\rangle$ and $|\downarrow\rangle$ of the spin z component (perpendicular to the monolayer). We assume that the Coulomb matrix in Wannier representation is spin independent and that spin-up and spin-down states are not mixed. Diagonalization of $H(\mathbf{k})$ yields the band structure $\varepsilon_{\mathbf{k}}^{\lambda}$ and the Bloch states $|\psi_{\mathbf{k}}^{\lambda}\rangle = \sum_{\alpha} c_{\alpha,\mathbf{k}}^{\lambda}|\mathbf{k}, \alpha\rangle$, where the coefficients $c_{\alpha,\mathbf{k}}^{\lambda}$ describe the momentum-dependent contribution of the orbital α to the Bloch band λ. The Bloch sums $|\mathbf{k}, \alpha\rangle$ are connected to the localized basis via $|\mathbf{k}, \alpha\rangle = (1/\sqrt{N}) \sum_{\mathbf{R}} e^{i\mathbf{k} \cdot \mathbf{R}}|\mathbf{R}, \alpha\rangle$ with the number of unit cells N and lattice vectors $\mathbf{R}$. The SOC Hamiltonian is given by

$$H_{\text{SOC}} = \frac{1}{\hbar^2}\tilde{L} \cdot S = \frac{1}{2\hbar}\tilde{L} \cdot \boldsymbol{\sigma} \tag{A2}$$

with the Pauli matrices $\boldsymbol{\sigma} = (\sigma_x, \sigma_y, \sigma_z)$ and the angular momentum operator provided in Ref. [20].

Starting from the density-density-like bare Coulomb interaction matrix elements in the Wannier basis,

$$U_{\alpha\beta}(\mathbf{q}) = \sum_{\mathbf{R}} e^{i\mathbf{q} \cdot \mathbf{R}} U_{\alpha\beta\beta\alpha}(\mathbf{R}) = \sum_{\mathbf{R}} e^{i\mathbf{q} \cdot \mathbf{R}} \langle \mathbf{0}, \alpha|\langle \mathbf{R}, \beta|U(\mathbf{r}, \mathbf{r}')|\mathbf{R}, \beta\rangle|\mathbf{0}, \alpha\rangle \tag{A3}$$

and the corresponding (statically) screened matrix elements $V_{\alpha\beta}(\mathbf{q})$, we obtain an analytic description of Coulomb interaction in freestanding transition metal dichalcogenide (TMD) heterobilayers that can be augmented by screening from a dielectric environment [8,67,68]. The parametrization of Coulomb matrix elements for a freestanding H_h^h MoSe$_2$/WSe$_2$ heterobilayer is provided in Ref. [20]. Environmental screening can be taken into account according to the Wannier function continuum electrostatics approach [69] that combines a macroscopic electrostatic model for the screening by the dielectric environment with a localized description of Coulomb interaction. The macroscopic dielectric function of a freestanding bilayer embedded in a vertical heterostructure is obtained by solving Poisson's equation [70].

We finally compute screened Coulomb matrix elements in the Bloch state representation by a unitary transformation using the coefficients $c_{\alpha,\mathbf{k}}^{\lambda}$:

$$V_{\mathbf{k}_1,\mathbf{k}_2,\mathbf{k}_3,\mathbf{k}_4}^{\lambda,\nu,\nu',\lambda'} = \frac{1}{\mathcal{A}} \sum_{\alpha,\beta} (c_{\alpha,\mathbf{k}_1}^{\lambda})^*(c_{\beta,\mathbf{k}_2}^{\nu})^* V_{\mathbf{k}_1-\mathbf{k}_4}^{\alpha\beta} c_{\beta,\mathbf{k}_3}^{\nu'} c_{\alpha,\mathbf{k}_4}^{\lambda'}, \tag{A4}$$

where $\mathbf{k}_4 = \mathbf{k}_1 + \mathbf{k}_2 - \mathbf{k}_3 + \mathbf{G}$ due to momentum conservation and $\mathcal{A}$ denotes the crystal area.

Inspired by the discussion in Ref. [71], we assume that Bloch states are approximately spin diagonal. We assign a definite spin to each band according to the dominant contribution given by the coefficients $c_{\alpha,\mathbf{k}}^{\lambda}$. Furthermore, we make use of the fact that Coulomb interaction is spin conserving, so that we can set Coulomb matrix elements $V_{\mathbf{k}_1\mathbf{k}_2\mathbf{k}_3\mathbf{k}_4}^{\lambda,\nu,\nu',\lambda'}$ to zero if λ and λ' or ν and ν' belong to different spins.

2. Derivation of a *GW* self-energy for excitons

We start from the definition of the exciton Schwinger-Keldysh Green function:

$$K(1,1') = \frac{1}{i\hbar}\langle\!\langle h_{\mathbf{k}_1}(\underline{t}_1)e_{\mathbf{p}_1}(\underline{t}_1)e'^{\dagger}_{\mathbf{p}'_1}(\underline{t}'_1)h'^{\dagger}_{\mathbf{k}'_1}(\underline{t}'_1)\rangle\!\rangle_T, \quad (A5)$$

which describes the creation of an electron-hole pair at time $\underline{t}'_1$ and annihilation at time $\underline{t}_1$. The notation $\langle\!\langle \cdot \rangle\!\rangle_T$ is short for the statistical average

$$\langle\!\langle \hat{A}(\underline{t})\rangle\!\rangle_T = \frac{\langle T_{\mathcal{C}}[S_{\mathcal{C}}\hat{A}(\underline{t})]\rangle}{\langle S_{\mathcal{C}}\rangle} \quad (A6)$$

with the time evolution operator

$$S_{\mathcal{C}} = T_{\mathcal{C}}\exp\left\{-\frac{i}{\hbar}\int_{\mathcal{C}}d\underline{t}'H_{\text{ext}}(\underline{t}')\right\} \quad (A7)$$

and $T_{\mathcal{C}}$ being the time-ordering operator on the Keldysh contour, which is depicted in Fig. 4. The Keldysh time coordinate $\underline{t}$ includes the branch index $n = \pm$ of the contour as well as the physical time coordinate t. The superindex 1 stands for electron momentum $\mathbf{p}_1$, hole momentum $\mathbf{k}_1$, electron band e, hole band h, and Keldysh time $\underline{t}_1$.
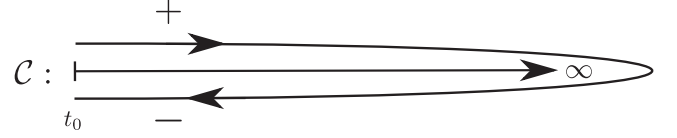

FIG. 4. The Keldysh contour $\mathcal{C}$ starts at initial time t_0, extends to ∞ on the upper branch $(+)$, and returns to t_0 on the lower branch $(-)$.

The band index also contains the spin quantum number. In Eq. (A5), the external Hamiltonian

$$H_{\text{ext}}(\underline{t}) = \frac{e}{\mathcal{A}}\sum_{\mathbf{k},\mathbf{k}',a,a'}V_{\text{ext}}^{a',a}(\mathbf{k},\mathbf{k}',\underline{t})\rho^{a',a}(\mathbf{k}',-\mathbf{k},\underline{t}) \quad (A8)$$

couples the time-dependent external potential V_{ext} to the particle-density operator

$$\rho^{a',a}(\mathbf{k}',\mathbf{k},\underline{t}) = s_a a'^{\dagger}_{\mathbf{k}'+\mathbf{k}}(\underline{t})a_{\mathbf{k}'}(\underline{t}). \quad (A9)$$

Here, we introduce the convention to assign a positive sign $s_a = +1$ to electrons $(a = e)$ and a negative sign $s_a = -1$ to holes $(a = h)$. Whenever densitylike operator pairs of the type in Eq. (A9) appear, it is understood that both band indices describe the same carrier species.

In the following, we derive an equation of motion (EOM) for the exciton Green function (A5) by means of Heisenberg's equation for operators in the interaction picture with respect to $H_{\text{ext}}(t)$:

$$i\hbar\frac{\partial}{\partial t}\hat{A}(t) = [\hat{A}(t),H], \quad (A10)$$

where the Hamiltonian describes the interacting gas of electrons and holes:

$$H = \sum_{\mathbf{p},e}\varepsilon_{\mathbf{p}}^e e_{\mathbf{p}}^{\dagger}e_{\mathbf{p}} + \sum_{\mathbf{k},h}\varepsilon_{\mathbf{k}}^h h_{\mathbf{k}}^{\dagger}h_{\mathbf{k}} + \frac{1}{2}\sum_{\mathbf{k},\mathbf{k}',\mathbf{q}}\sum_{e,e',a,a'}s_e s_a V_{\mathbf{k},\mathbf{k}',\mathbf{k}'+\mathbf{q},\mathbf{k}-\mathbf{q}}^{e,a,a',e'}e_{\mathbf{k}}^{\dagger}a_{\mathbf{k}'}^{\dagger}a_{\mathbf{k}'+\mathbf{q}}e'_{\mathbf{k}-\mathbf{q}}$$
$$+\frac{1}{2}\sum_{\mathbf{k},\mathbf{k}',\mathbf{q}}\sum_{h,h',a,a'}s_h s_a V_{\mathbf{k},\mathbf{k}',\mathbf{k}'+\mathbf{q},\mathbf{k}-\mathbf{q}}^{h,a,a',h'}h_{\mathbf{k}}^{\dagger}a_{\mathbf{k}'}^{\dagger}a_{\mathbf{k}'+\mathbf{q}}h'_{\mathbf{k}-\mathbf{q}}. \quad (A11)$$

Hole energies and wave functions are obtained from the valence-band quantities as $\varepsilon_{\mathbf{k}}^h = -\varepsilon_{\mathbf{k}}^v$ and $c_{\alpha,\mathbf{k}}^h = (c_{\alpha,\mathbf{k}}^v)^*$. The EOM for creation and annihilation operators can be derived using

$$[\hat{A}\,\hat{B},\hat{C}] = \hat{A}[\hat{B},\hat{C}]_+ - [\hat{A},\hat{C}]_+\hat{B}, \quad (A12)$$

with the anticommutator $[\cdot,\cdot]_+$. To proceed, we apply the time-ordering operator in Eq. (A5):

$$i\hbar\frac{\partial}{\partial t_1}K(1,1') = \frac{\partial}{\partial t_1}\left\{\theta_{\mathcal{C}}(\underline{t}_1,\underline{t}'_1)\langle\!\langle h_{\mathbf{k}_1}(\underline{t}_1)e_{\mathbf{p}_1}(\underline{t}_1)e'^{\dagger}_{\mathbf{p}'_1}(\underline{t}'_1)h'^{\dagger}_{\mathbf{k}'_1}(\underline{t}'_1)\rangle\!\rangle + \theta_{\mathcal{C}}(\underline{t}'_1,\underline{t}_1)\langle\!\langle h'^{\dagger}_{\mathbf{k}'_1}(\underline{t}'_1)e'^{\dagger}_{\mathbf{p}'_1}(\underline{t}'_1)e_{\mathbf{p}_1}(\underline{t}_1)h_{\mathbf{k}_1}(\underline{t}_1)\rangle\!\rangle\right\}, \quad (A13)$$

where the step function on the Keldysh contour is introduced as $\theta_{\mathcal{C}}(\underline{t}_1,\underline{t}_2) = \delta_{n_1,-} + n_1\delta_{n_1,n_2}\theta(t_1 - t_2)$ to take all four combinations of branch indices n_1 and n_2 into account correctly. We use brackets $\langle\!\langle \cdot \rangle\!\rangle$ to denote the statistical average (A6)

without time ordering. The time derivative of expectation values is evaluated by splitting the exponential in S_C according to the Keldysh time ordering. Then, we obtain

$$
i\hbar \frac{\partial}{\partial t_1} K(1,1') = n_1 \delta_{n_1,n_1'} \delta(t_1 - t_1') F(1,1') + (\varepsilon_{\mathbf{p}}^e + \varepsilon_{\mathbf{k}}^h) K(1,1') + \frac{e}{\mathcal{A}} \sum_{\mathbf{k}} \left\{ \sum_{e''} V_{\text{ext}}^{e,e''}(\mathbf{p}_1 + \mathbf{k}, \mathbf{k}, \underline{t}_1) K(1,1') \bigg|_{\mathbf{p}_1 + \mathbf{k}, e''} \right.
$$

$$
\left. - \sum_{h''} V_{\text{ext}}^{h,h''}(\mathbf{k}_1 + \mathbf{k}, \mathbf{k}, \underline{t}_1) K(1,1') \bigg|_{\mathbf{k}_1 + \mathbf{k}, h''} \right\} - \sum_{\mathbf{q}, h'', e''} V_{\mathbf{p}_1, \mathbf{k}_1, \mathbf{k}_1 + \mathbf{q}, \mathbf{p}_1 - \mathbf{q}}^{e,h,h'',e''} K(1,1') \bigg|_{\mathbf{p}_1 - \mathbf{q}, e''}^{\mathbf{k}_1 + \mathbf{q}, h''}
$$

$$
+ \sum_{\mathbf{k}, \mathbf{q}, a, a', h''} s_h s_a V_{\mathbf{k}_1, \mathbf{k}, \mathbf{k}+\mathbf{q}, \mathbf{k}_1 - \mathbf{q}}^{h,a,a',h''} r(1, 1', \mathbf{k}, \mathbf{q}, a, a', \underline{t}_1^+) \bigg|_{\mathbf{k}_1 - \mathbf{q}, h''}
$$

$$
+ \sum_{\mathbf{k}, \mathbf{q}, a, a', e''} s_e s_a V_{\mathbf{p}_1, \mathbf{k}, \mathbf{k}+\mathbf{q}, \mathbf{p}_1 - \mathbf{q}}^{e,a,a',e''} r(1, 1', \mathbf{k}, \mathbf{q}, a, a', \underline{t}_1^+) \bigg|_{\mathbf{p}_1 - \mathbf{q}, e''} \tag{A14}
$$

with the phase-space filling factor

$$
F(1,1') = \langle\!\langle \hat{F}(1,1') \rangle\!\rangle = \delta_{\mathbf{k}_1, \mathbf{k}_1'} \delta_{\mathbf{p}_1, \mathbf{p}_1'} \delta_{h,h'} \delta_{e,e'} - \delta_{\mathbf{p}_1, \mathbf{p}_1'} \delta_{e,e'} \langle\!\langle h_{\mathbf{k}_1'}^\dagger(\underline{t}_1) h_{\mathbf{k}_1}(\underline{t}_1) \rangle\!\rangle - \delta_{\mathbf{k}_1, \mathbf{k}_1'} \delta_{h,h'} \langle\!\langle e_{\mathbf{p}_1'}'^\dagger(\underline{t}_1) e_{\mathbf{p}_1}(\underline{t}_1) \rangle\!\rangle \tag{A15}
$$

and the three-particle Green function

$$
r(1, 1', \mathbf{k}, \mathbf{q}, a, a', \underline{t}) = \frac{1}{i\hbar} \langle\!\langle a_{\mathbf{k}}^\dagger(\underline{t}^+) a'_{\mathbf{k}+\mathbf{q}}(\underline{t}) h_{\mathbf{k}_1}(\underline{t}_1) e_{\mathbf{p}_1}(\underline{t}_1) e_{\mathbf{p}_1'}'^\dagger(\underline{t}_1') h_{\mathbf{k}_1'}'^\dagger(\underline{t}_1') \rangle\!\rangle_T. \tag{A16}
$$

Here, $\underline{t}^+$ denotes a time that is infinitesimally later on the Keldysh contour than $\underline{t}$. We also introduce the notation $K(1,1')|_{\mathbf{k}_1 + \mathbf{q}, h''(\mathbf{p}_1 + \mathbf{q}, e'')}$ for a Green function where the hole state (electron state) of argument 1 is changed. By introducing the free inverse exciton Green function

$$
K_0^{-1}(1,1') = n_1 \delta_{n_1,n_1'} \delta(t_1 - t_1') \left\{ i\hbar \frac{\partial}{\partial t_1} \delta_{\mathbf{k}_1, \mathbf{k}_1'} \delta_{\mathbf{p}_1, \mathbf{p}_1'} \delta_{h,h'} \delta_{e,e'} - \mathcal{H}_0(1,1') - V_{\text{ext}}(1,1', \underline{t}_1) \right\} \tag{A17}
$$

with the effective exciton Hamiltonian

$$
\mathcal{H}_0(1,1') = (\varepsilon_{\mathbf{p}}^e + \varepsilon_{\mathbf{k}}^h) \delta_{\mathbf{k}_1, \mathbf{k}_1'} \delta_{\mathbf{p}_1, \mathbf{p}_1'} \delta_{h,h'} \delta_{e,e'} - \sum_{\mathbf{q}, h'', e''} V_{\mathbf{p}_1, \mathbf{k}_1, \mathbf{k}_1 + \mathbf{q}, \mathbf{p}_1 - \mathbf{q}}^{e,h,h'',e''} \delta_{\mathbf{k}_1 + \mathbf{q}, \mathbf{k}_1'} \delta_{\mathbf{p}_1 - \mathbf{q}, \mathbf{p}_1'} \delta_{h'',h'} \delta_{e'',e'} \tag{A18}
$$

and the external potential

$$
V_{\text{ext}}(1,1',\underline{t}_1) = \frac{e}{\mathcal{A}} \sum_{\mathbf{k}} \left\{ \sum_{e''} V_{\text{ext}}^{e,e''}(\mathbf{p}_1 + \mathbf{k}, \mathbf{k}, \underline{t}_1) \delta_{\mathbf{k}_1, \mathbf{k}_1'} \delta_{\mathbf{p}_1 + \mathbf{k}, \mathbf{p}_1'} \delta_{h,h'} \delta_{e'',e'} - \sum_{h''} V_{\text{ext}}^{h,h''}(\mathbf{k}_1 + \mathbf{k}, \mathbf{k}, \underline{t}_1) \delta_{\mathbf{k}_1 + \mathbf{k}, \mathbf{k}_1'} \delta_{\mathbf{p}_1, \mathbf{p}_1'} \delta_{h'',h'} \delta_{e,e'} \right\},
$$

$$
\tag{A19}
$$

we bring the EOM (A14) to its integral form:

$$
\int_{\mathcal{C}} d\underline{t}_2 \sum_{\mathbf{k}_2, \mathbf{p}_2, h_2, e_2} K_0^{-1}(1,2) K(2,1') = n_1 \delta_{n_1,n_1'} \delta(t_1 - t_1') F(1,1') + \sum_{\mathbf{k}, \mathbf{q}, a, a', h''} s_h s_a V_{\mathbf{k}_1, \mathbf{k}, \mathbf{k}+\mathbf{q}, \mathbf{k}_1 - \mathbf{q}}^{h,a,a',h''} r(1, 1', \mathbf{k}, \mathbf{q}, a, a', \underline{t}_1^+) \bigg|_{\mathbf{k}_1 - \mathbf{q}, h''}
$$

$$
+ \sum_{\mathbf{k}, \mathbf{q}, a, a', e''} s_e s_a V_{\mathbf{p}_1, \mathbf{k}, \mathbf{k}+\mathbf{q}, \mathbf{p}_1 - \mathbf{q}}^{e,a,a',e''} r(1, 1', \mathbf{k}, \mathbf{q}, a, a', \underline{t}_1^+) \bigg|_{\mathbf{p}_1 - \mathbf{q}, e''}. \tag{A20}
$$

The exciton Green function is coupled via Coulomb interaction to three-particle Green functions, which, in turn, are coupled to four-particle Green functions and so forth. To truncate this hierarchy of EOM, we eliminate the three-particle Green function in Eq. (A20) by using the functional derivative with respect to the external potential, which is contained in the time evolution operator:

$$\frac{\delta K(1,1')}{\delta V_{\text{ext}}^{b',b}(\mathbf{q}',\mathbf{q},\underline{t})} = \frac{e}{\mathcal{A}}\left\{s_b \frac{1}{i\hbar} r(1,1',\mathbf{q}'-\mathbf{q},\mathbf{q},b',b,\underline{t}) - K(1,1')d^{b',b}(\mathbf{q}',-\mathbf{q},\underline{t})\right\} \tag{A21}$$

with $d^{b',b}(\mathbf{q}',-\mathbf{q},\underline{t}) = (1/i\hbar)\langle\!\langle \rho^{b',b}(\mathbf{q}',-\mathbf{q},\underline{t})\rangle\!\rangle$. The integral EOM (A20) is then written as

$$\int_{\mathcal{C}} d\underline{t}_2 \sum_{\mathbf{k}_2,\mathbf{p}_2,h_2,e_2} K_{\text{eff}}^{-1}(1,2)K(2,1')$$

$$= n_1\delta_{n_1,n_1'}\delta(t_1-t_1')F(1,1') + i\hbar\frac{\mathcal{A}}{e}\sum_{\mathbf{k},\mathbf{q},a,a'}\left\{\sum_{e''}V_{\mathbf{p}_1,\mathbf{k},\mathbf{k}+\mathbf{q},\mathbf{p}_1-\mathbf{q}}^{e,a,a',e''}\frac{\delta K(1,1')|_{\mathbf{p}_1-\mathbf{q},e''}}{\delta V_{\text{ext}}^{a,a'}(\mathbf{k}+\mathbf{q},\mathbf{q},\underline{t}_1^+)} - \sum_{h''}V_{\mathbf{k}_1,\mathbf{k},\mathbf{k}+\mathbf{q},\mathbf{k}_1-\mathbf{q}}^{h,a,a',h''}\frac{\delta K(1,1')|_{\mathbf{k}_1-\mathbf{q},h''}}{\delta V_{\text{ext}}^{a,a'}(\mathbf{k}+\mathbf{q},\mathbf{q},\underline{t}_1^+)}\right\}. \tag{A22}$$

The operator $K_{\text{eff}}^{-1}(1,2)$ follows from $K_0^{-1}(1,2)$ if the external potential V_{ext} is replaced by the effective potential V_{eff} that also contains the electrostatic potential of the mean charge density:

$$V_{\text{eff}}^{a,a'}(\mathbf{k}+\mathbf{q},\mathbf{q},\underline{t}_1) = V_{\text{ext}}^{a,a'}(\mathbf{k}+\mathbf{q},\mathbf{q},\underline{t}_1) + \frac{\mathcal{A}}{e}\sum_{\mathbf{k}',b,b'}V_{\mathbf{k},\mathbf{k}',\mathbf{k}'-\mathbf{q},\mathbf{k}+\mathbf{q}}^{a,b,b',a'}\rho^{b,b'}(\mathbf{k}'-\mathbf{q},\mathbf{q},\underline{t}_1). \tag{A23}$$

We exploit the chain rule for functional derivatives to reformulate the interaction term on the rhs of Eq. (A22):

$$\frac{\delta K(1,1')}{\delta V_{\text{ext}}^{a,a'}(\mathbf{k}+\mathbf{q},\mathbf{q},\underline{t}_1^+)} = \int_{\mathcal{C}} d\underline{t}_2 \sum_{\mathbf{k}_2,\mathbf{q}_2,a_2,a_2'}\frac{\delta K(1,1')}{\delta V_{\text{eff}}^{a_2,a_2'}(\mathbf{k}_2+\mathbf{q}_2,\mathbf{q}_2,\underline{t}_2)}\frac{\delta V_{\text{eff}}^{a_2,a_2'}(\mathbf{k}_2+\mathbf{q}_2,\mathbf{q}_2,\underline{t}_2)}{\delta V_{\text{ext}}^{a,a'}(\mathbf{k}+\mathbf{q},\mathbf{q},\underline{t}_1^+)}. \tag{A24}$$

The second factor is identified as the inverse dielectric function

$$\varepsilon^{-1}(\mathbf{k}_2+\mathbf{q}_2,\mathbf{q}_2,a_2,a_2',\underline{t}_2,\mathbf{k}+\mathbf{q},\mathbf{q},a,a',\underline{t}_1) = \frac{\delta V_{\text{eff}}^{a_2,a_2'}(\mathbf{k}_2+\mathbf{q}_2,\mathbf{q}_2,\underline{t}_2)}{\delta V_{\text{ext}}^{a,a'}(\mathbf{k}+\mathbf{q},\mathbf{q},\underline{t}_1)}$$

$$= n_1\delta_{n_1,n_2}\delta(t_1-t_2)\delta_{\mathbf{k},\mathbf{k}_2}\delta_{\mathbf{q},\mathbf{q}_2}\delta_{a,a_2}\delta_{a',a_2'}$$

$$+ \sum_{\mathbf{k}',b,b'}V_{\mathbf{k}_2,\mathbf{k}',\mathbf{k}'-\mathbf{q}_2,\mathbf{k}_2+\mathbf{q}_2}^{a_2,b,b',a_2'}\left\{L(\mathbf{k}'-\mathbf{q}_2,\mathbf{q}_2,b,b',\underline{t}_2,\mathbf{k}+\mathbf{q},-\mathbf{q},a,a',\underline{t}_1)\right.$$

$$\left. - i\hbar d^{b,b'}(\mathbf{k}'-\mathbf{q}_2,\mathbf{q}_2,\underline{t}_2))d^{a,a'}(\mathbf{k}+\mathbf{q},-\mathbf{q},\underline{t}_1)\right\} \tag{A25}$$

with the density-density expectation value

$$L(\mathbf{k}'-\mathbf{q}_2,\mathbf{q}_2,b,b',\underline{t}_2,\mathbf{k}+\mathbf{q},-\mathbf{q},a,a',\underline{t}_1) = \frac{1}{i\hbar}\langle\!\langle \rho^{a,a'}(\mathbf{k}+\mathbf{q},-\mathbf{q},\underline{t}_1)\rho^{b,b'}(\mathbf{k}'-\mathbf{q}_2,\mathbf{q}_2,\underline{t}_2)\rangle\!\rangle_T. \tag{A26}$$

Also, by defining the inverse exciton Green function via

$$\int_{\mathcal{C}} d\underline{t}_2 \sum_{\mathbf{k}_2,\mathbf{p}_2,h_2,e_2} K^{-1}(1,2)K(2,1') = n_1\delta_{n_1,n_1'}\delta(t_1-t_1')\delta_{\mathbf{k}_1,\mathbf{k}_1'}\delta_{\mathbf{p}_1,\mathbf{p}_1'}\delta_{h,h'}\delta_{e,e'}, \tag{A27}$$

we find for the polarization function

$$\Pi(3,1',\mathbf{k}_4+\mathbf{q}_4,\mathbf{q}_4,a_4,a_4',\underline{t}_4) = \frac{\delta K(3,1')}{\delta V_{\text{eff}}^{a_4,a_4'}(\mathbf{k}_4+\mathbf{q}_4,\mathbf{q}_4,\underline{t}_4)}$$

$$= \frac{e}{\mathcal{A}}\int_{\mathcal{C}} d\underline{t}_1 \int_{\mathcal{C}} d\underline{t}_2 \sum_{\mathbf{k}_1,\mathbf{p}_1,h_1,e_1}\sum_{\mathbf{k}_2,\mathbf{p}_2,h_2,e_2}K(3,1)\Gamma(1,2,\mathbf{k}_4+\mathbf{q}_4,\mathbf{q}_4,a_4,a_4',\underline{t}_4)K(2,1') \tag{A28}$$

with the vertex function

$$\Gamma(1,2,\mathbf{k}_4+\mathbf{q}_4,\mathbf{q}_4,a_4,a_4',\underline{t}_4) = -\frac{\mathcal{A}}{e}\frac{\delta K^{-1}(1,2)}{\delta V_{\text{eff}}^{a_4,a_4'}(\mathbf{k}_4+\mathbf{q}_4,\mathbf{q}_4,\underline{t}_4)}. \tag{A29}$$

Combining Eqs. (A22), (A24), (A25), and (A28), we arrive at the Dyson equation for the exciton Green function:

$$
\int_{\mathcal{C}} d\underline{t}_2 \sum_{\mathbf{k}_2,\mathbf{p}_2,h_2,e_2} K_{\text{eff}}^{-1}(1,2)K(2,1')
$$

$$
= n_1 \delta_{n_1,n_1'} \delta(t_1 - t_1') F(1,1') + i\hbar \sum_{\mathbf{k},\mathbf{q},a,a'} \int_{\mathcal{C}} d\underline{t}_2 \sum_{\mathbf{k}_2,\mathbf{q}_2,a_2,a_2'} \varepsilon^{-1}(\mathbf{k}_2 + \mathbf{q}_2, \mathbf{q}_2, a_2, a_2', \underline{t}_2, \mathbf{k} + \mathbf{q}, \mathbf{q}, a, a', \underline{t}_1)
$$

$$
\times \int_{\mathcal{C}} d\underline{t}_3 \sum_{\mathbf{k}_3,\mathbf{p}_3,h_3,e_3} \left\{ \sum_{e''} V_{\mathbf{p}_1,\mathbf{k},\mathbf{k}+\mathbf{q},\mathbf{p}_1-\mathbf{q}}^{e,a,a',e''} K(1,3)|_{\mathbf{p}_1-\mathbf{q},e''} - \sum_{h''} V_{\mathbf{k}_1,\mathbf{k},\mathbf{k}+\mathbf{q},\mathbf{k}_1-\mathbf{q}}^{h,a,a',h''} K(1,3) \Big|_{\mathbf{k}_1-\mathbf{q},h''} \right\}
$$

$$
\times \int_{\mathcal{C}} d\underline{t}_4 \sum_{\mathbf{k}_4,\mathbf{p}_4,h_4,e_4} \Gamma(3,4,\mathbf{k}_2 + \mathbf{q}_2, \mathbf{q}_2, a_2, a_2', \underline{t}_2) K(4,1')
$$

$$
= n_1 \delta_{n_1,n_1'} \delta(t_1 - t_1') F(1,1') + \int_{\mathcal{C}} d\underline{t}_4 \sum_{\mathbf{k}_4,\mathbf{p}_4,h_4,e_4} \Sigma(1,4) K(4,1') \tag{A30}
$$

with the self-energy $\Sigma(1,1')$. Equation (A30) is an exact EOM for the exciton Green function, where the many-body interaction effects are contained in the self-energy or, more specifically, in the inverse dielectric function and the vertex function. To solve the many-body problem for the dense exciton gas, approximations have to be applied to the self-energy.

We derive the lowest approximation to the vertex function (A29) by neglecting the density terms in the phase-space filling factor $F(1,1')$ and inverting Eq. (A30) to obtain an EOM for the inverse exciton Green function:

$$
K^{-1}(1,1') = K_{\text{eff}}^{-1}(1,1') - \Sigma(1,1'). \tag{A31}
$$

The derivative of $K_{\text{eff}}^{-1}(1,1')$ with respect to V_{eff} then yields a deltalike vertex function:

$$
\Gamma(3,4,\mathbf{k}_2 + \mathbf{q}_2, \mathbf{q}_2, a_2, a_2', \underline{t}_2) \approx n_3 \delta_{n_3,n_4} \delta(t_3 - t_4) n_3 \delta_{n_3,n_2} \delta(t_3 - t_2)
$$

$$
\times \left\{ \delta_{\mathbf{k}_3,\mathbf{k}_4} \delta_{\mathbf{p}_3+\mathbf{q}_2,\mathbf{p}_4} \delta_{\mathbf{k}_2,\mathbf{p}_3} \delta_{h_3,h_4} \delta_{a_2,e_3} \delta_{a_2',e_4} - \delta_{\mathbf{p}_3,\mathbf{p}_4} \delta_{\mathbf{k}_3+\mathbf{q}_2,\mathbf{k}_4} \delta_{\mathbf{k}_2,\mathbf{k}_3} \delta_{e_3,e_4} \delta_{a_2,h_3} \delta_{a_2',h_4} \right\}. \tag{A32}
$$

Inserting this into Eq. (A30), we obtain the self-energy in random-phase approximation (RPA):

$$
\Sigma(1,1') = i\hbar \sum_{\mathbf{k},\mathbf{q},\mathbf{q}_2,a,a'} \left\{ \sum_{\bar{e}} \varepsilon^{-1}(\mathbf{p}_1', \mathbf{q}_2, \bar{e}, e', \underline{t}_1', \mathbf{k} + \mathbf{q}, \mathbf{q}, a, a', \underline{t}_1^+) \right.
$$

$$
\times \left(\sum_{e''} V_{\mathbf{p}_1,\mathbf{k},\mathbf{k}+\mathbf{q},\mathbf{p}_1-\mathbf{q}}^{e,a,a',e''} K(1,1') \Big|_{\mathbf{p}_1'-\mathbf{q}_2,\bar{e}}^{\mathbf{p}_1-\mathbf{q},e''} - \sum_{h''} V_{\mathbf{k}_1,\mathbf{k},\mathbf{k}+\mathbf{q},\mathbf{k}_1-\mathbf{q}}^{h,a,a',h''} K(1,1') \Big|_{\mathbf{p}_1'-\mathbf{q}_2,\bar{e}}^{\mathbf{k}_1-\mathbf{q},h''} \right)
$$

$$
+ \sum_{\bar{h}} \varepsilon^{-1}(\mathbf{k}_1', \mathbf{q}_2, \bar{h}, h', \underline{t}_1', \mathbf{k} + \mathbf{q}, \mathbf{q}, a, a', \underline{t}_1^+)
$$

$$
\times \left. \left(\sum_{h''} V_{\mathbf{k}_1,\mathbf{k},\mathbf{k}+\mathbf{q},\mathbf{k}_1-\mathbf{q}}^{h,a,a',h''} K(1,1') \Big|_{\mathbf{k}_1'-\mathbf{q}_2,\bar{h}}^{\mathbf{k}_1-\mathbf{q},h''} - \sum_{e''} V_{\mathbf{p}_1,\mathbf{k},\mathbf{k}+\mathbf{q},\mathbf{p}_1-\mathbf{q}}^{e,a,a',e''} K(1,1') \Big|_{\mathbf{k}_1'-\mathbf{q}_2,\bar{h}}^{\mathbf{p}_1-\mathbf{q},e''} \right) \right\}. \tag{A33}
$$

The matrix elements V contain background screening from the filled valence bands as well as from the dielectric environment. On the other hand, the inverse dielectric function ε^{-1} describes screening from photoexcited electrons and holes. Therefore, the (matrix) product $\varepsilon^{-1}V$ can be identified as the fully screened Coulomb interaction W, which gives the self-energy (A33) the well-known GW form. As main difference to the standard GW self-energy, its excitonic version contains four interaction terms between the electrons and holes constituting two interacting excitons. Note that Coulomb interaction between the electron and hole within the same exciton is already included in the free inverse exciton Green function (A17). However, as discussed in Ref. [34], the RPA self-energy does not describe effects due to the exchange of fermions *between* two excitons. In the following subsection, we again follow Ref. [34] to derive such fermionic corrections to the GW self-energy.

3. Exchange corrections to the GW self-energy

Instead of eliminating the three-particle Green function r by means of functional derivatives from the EOM of the exciton Green function (A14), we derive an EOM for r itself using an alternative decoupling mechanism. To this end, we make use of the free inverse exciton Green function (A17):

$$\int_{\mathcal{C}} dt_2 \sum_{\mathbf{k}_2,\mathbf{p}_2,h_2,e_2} r(1,2,\mathbf{k},\mathbf{q},a,a',\underline{t}_1^+) K_0^{-1}(2,1')$$

$$= \int_{\mathcal{C}} dt_2 \sum_{\mathbf{k}_2,\mathbf{p}_2,h_2,e_2} r(1,2,\mathbf{k},\mathbf{q},a,a',\underline{t}_1^+) n_2 \delta_{n_2,n_1'} \delta(t_2 - t_1') \left\{ i\hbar \frac{\partial}{\partial t_2} \delta_{\mathbf{k}_2,\mathbf{k}_1'} \delta_{\mathbf{p}_2,\mathbf{p}_1'} \delta_{h_2,h'} \delta_{e_2,e'} - \mathcal{H}_0(2,1') - V_{\text{ext}}(2,1',\underline{t}_2) \right\}. \quad \text{(A34)}$$

Since K_0^{-1} acts to the left, we have to apply the adjoint operators in each term. The time derivative

$$-i\hbar \frac{\partial}{\partial t_1'} r(1,1',\mathbf{k},\mathbf{q},a,a',\underline{t}_1^+) = -\frac{\partial}{\partial t_1'} \left\{ \theta_{\mathcal{C}}(\underline{t}_1,\underline{t}_1') \langle\!\langle a_{\mathbf{k}}^\dagger(\underline{t}_1) a'_{\mathbf{k}+\mathbf{q}}(\underline{t}_1) h_{\mathbf{k}_1}(\underline{t}_1) e_{\mathbf{p}_1}(\underline{t}_1) e_{\mathbf{p}_1'}'^\dagger(\underline{t}_1') h_{\mathbf{k}_1'}'^\dagger(\underline{t}_1') \rangle\!\rangle \right.$$
$$\left. + \theta_{\mathcal{C}}(\underline{t}_1',\underline{t}_1) \langle\!\langle e_{\mathbf{p}_1'}'^\dagger(\underline{t}_1') h_{\mathbf{k}_1'}'^\dagger(\underline{t}_1') a_{\mathbf{k}}^\dagger(\underline{t}_1) a'_{\mathbf{k}+\mathbf{q}}(\underline{t}_1) h_{\mathbf{k}_1}(\underline{t}_1) e_{\mathbf{p}_1}(\underline{t}_1) \rangle\!\rangle \right\} \quad \text{(A35)}$$

is evaluated along the same lines as for the two-particle Green function (A13). Note that, in Eq. (A35), the time derivative is acting on creation instead of annihilation operators. Multiplying Eq. (A34) with $K_0(1',3)$ from the right, integrating over the superindex $1'$, and using the relation

$$\int_{\mathcal{C}} dt_2 \sum_{\mathbf{k}_2,\mathbf{p}_2,h_2,e_2} K_0^{-1}(1,2) K_0(2,1') = n_1 \delta_{n_1,n_1'} \delta(t_1 - t_1') \delta_{\mathbf{k}_1,\mathbf{k}_1'} \delta_{\mathbf{p}_1,\mathbf{p}_1'} \delta_{h,h'} \delta_{e,e'}, \quad \text{(A36)}$$

we arrive at the following explicit expression for r:

$$r(1,3,\mathbf{k},\mathbf{q},a,a',\underline{t}_1^+) = \int_{\mathcal{C}} dt_1' \sum_{\mathbf{k}_1',\mathbf{p}_1',h',e'} r_0(1,1',\mathbf{k},\mathbf{q},a,a',\underline{t}_1^+) K_0(1',3) + \int_{\mathcal{C}} dt_1' \sum_{\mathbf{k}_1',\mathbf{p}_1',h',e'} \sum_{\mathbf{k}',\mathbf{q}',a'',a'''}$$

$$\times \left\{ \sum_{h''} s_{h'} s_{a''} V_{\mathbf{k}_1'+\mathbf{q}',\mathbf{k}',\mathbf{k}'+\mathbf{q}',\mathbf{k}_1'}^{h'',a'',a''',h'} s(1,1',\mathbf{k},\mathbf{q},a,a',\underline{t}_1,\mathbf{k}',\mathbf{q}',a'',a''',\underline{t}_1') \Big|_{\mathbf{k}_1'+\mathbf{q}',h''} \right.$$

$$\left. \times \sum_{e''} s_{e'} s_{a''} V_{\mathbf{p}_1'+\mathbf{q}',\mathbf{k}',\mathbf{k}'+\mathbf{q}',\mathbf{p}_1'}^{e'',a'',a''',e'} s(1,1',\mathbf{k},\mathbf{q},a,a',\underline{t}_1,\mathbf{k}',\mathbf{q}',a'',a''',\underline{t}_1') \Big|_{\mathbf{p}_1'+\mathbf{q}',e''} \right\} K_0(1',3). \quad \text{(A37)}$$

Here, r_0 results from the time derivative of the theta functions in Eq. (A35), for which we find

$$r_0(1,1',\mathbf{k},\mathbf{q},a,a',\underline{t}_1^+) = n_1 \delta_{n_1,n_1'} \delta(t_1 - t_1') \langle\!\langle [a_{\mathbf{k}}^\dagger(\underline{t}_1) a'_{\mathbf{k}+\mathbf{q}}(\underline{t}_1) h_{\mathbf{k}_1}(\underline{t}_1) e_{\mathbf{p}_1}(\underline{t}_1), e_{\mathbf{p}_1'}'^\dagger(\underline{t}_1) h_{\mathbf{k}_1'}'^\dagger(\underline{t}_1)] \rangle\!\rangle$$

$$= n_1 \delta_{n_1,n_1'} \delta(t_1 - t_1') \left\{ \langle\!\langle a_{\mathbf{k}}^\dagger(\underline{t}_1) a'_{\mathbf{k}+\mathbf{q}}(\underline{t}_1) \hat{F}(1,1') \rangle\!\rangle \right.$$

$$\left. + \delta_{\mathbf{p}_1',\mathbf{k}+\mathbf{q}} \delta_{e',a'} \langle\!\langle a_{\mathbf{k}}^\dagger(\underline{t}_1) h_{\mathbf{k}_1'}'^\dagger(\underline{t}_1) h_{\mathbf{k}_1}(\underline{t}_1) e_{\mathbf{p}_1}(\underline{t}_1) \rangle\!\rangle + \delta_{\mathbf{k}_1',\mathbf{k}+\mathbf{q}} \delta_{h',a'} \langle\!\langle e_{\mathbf{p}_1'}'^\dagger(\underline{t}_1) a_{\mathbf{k}}^\dagger(\underline{t}_1) h_{\mathbf{k}_1}(\underline{t}_1) e_{\mathbf{p}_1}(\underline{t}_1) \rangle\!\rangle \right\}. \quad \text{(A38)}$$

The three-particle Green function couples to four-particle Green functions of the type

$$s(1,1',\mathbf{k},\mathbf{q},a,a',\underline{t},\mathbf{k}',\mathbf{q}',a'',a''',\underline{t}') = \frac{1}{i\hbar} \langle\!\langle a_{\mathbf{k}}^\dagger(\underline{t}^+) a'_{\mathbf{k}+\mathbf{q}}(\underline{t}) h_{\mathbf{k}_1}(\underline{t}_1) e_{\mathbf{p}_1}(\underline{t}_1) e_{\mathbf{p}_1'}'^\dagger(\underline{t}_1') h_{\mathbf{k}_1'}'^\dagger(\underline{t}_1') a_{\mathbf{k}'}''^\dagger(\underline{t}'^+) a'''_{\mathbf{k}'+\mathbf{q}'}(\underline{t}') \rangle\!\rangle_T. \quad \text{(A39)}$$

The expression (A37) is inserted in the EOM for the two-particle Green function (A20), which yields

$$\int_{\mathcal{C}} dt_2 \sum_{\mathbf{k}_2,\mathbf{p}_2,h_2,e_2} K_0^{-1}(1,2) K(2,1') = n_1 \delta_{n_1,n_1'} \delta(t_1 - t_1') F(1,1') + \int_{\mathcal{C}} dt_2 \sum_{\mathbf{k}_2,\mathbf{p}_2,h_2,e_2} M(1,2) K_0(2,1') \quad \text{(A40)}$$

with

$$M(1, 1') = \sum_{\mathbf{k},\mathbf{q},a,a'} \left\{ \sum_{\bar{h}} s_a s_h V^{h,a,a',\bar{h}}_{\mathbf{k}_1,\mathbf{k},\mathbf{k}+\mathbf{q},\mathbf{k}_1-\mathbf{q}} \left(r_0(1, 1', \mathbf{k}, \mathbf{q}, a, a', \underline{t}_1^+) \Big|_{\mathbf{k}_1-\mathbf{q},\bar{h}} \right. \right.$$

$$+ \sum_{\mathbf{k}',\mathbf{q}',a'',a'''} \left\{ \sum_{h''} s_{h'} s_{a''} V^{h'',a'',a''',h'}_{\mathbf{k}_1'+\mathbf{q}',\mathbf{k}',\mathbf{k}'+\mathbf{q}',\mathbf{k}_1'} s(1, 1', \mathbf{k}, \mathbf{q}, a, a', \underline{t}_1, \mathbf{k}', \mathbf{q}', a'', a''', \underline{t}_1') \Big|^{\mathbf{k}_1-\mathbf{q},\bar{h}}_{\mathbf{k}_1'+\mathbf{q}',h''} \right.$$

$$+ \sum_{e''} s_{e'} s_{a''} V^{e'',a'',a''',e'}_{\mathbf{p}_1'+\mathbf{q}',\mathbf{k}',\mathbf{k}'+\mathbf{q}',\mathbf{p}_1'} s(1, 1', \mathbf{k}, \mathbf{q}, a, a', \underline{t}_1, \mathbf{k}', \mathbf{q}', a'', a''', \underline{t}_1') \Big|^{\mathbf{k}_1-\mathbf{q},\bar{h}}_{\mathbf{p}_1'+\mathbf{q}',e''} \right\} \Bigg)$$

$$+ \sum_{\bar{e}} s_a s_e V^{e,a,a',\bar{e}}_{\mathbf{p}_1,\mathbf{k},\mathbf{k}+\mathbf{q},\mathbf{p}_1-\mathbf{q}} \left(r_0(1, 1', \mathbf{k}, \mathbf{q}, a, a', \underline{t}_1^+) \Big|_{\mathbf{p}_1-\mathbf{q},\bar{e}} \right.$$

$$+ \sum_{\mathbf{k}',\mathbf{q}',a'',a'''} \left\{ \sum_{h''} s_{h'} s_{a''} V^{h'',a'',a''',h'}_{\mathbf{k}_1'+\mathbf{q}',\mathbf{k}',\mathbf{k}'+\mathbf{q}',\mathbf{k}_1'} s(1, 1', \mathbf{k}, \mathbf{q}, a, a', \underline{t}_1, \mathbf{k}', \mathbf{q}', a'', a''', \underline{t}_1') \Big|^{\mathbf{p}_1-\mathbf{q},\bar{e}}_{\mathbf{k}_1'+\mathbf{q}',h''} \right.$$

$$+ \sum_{e''} s_{e'} s_{a''} V^{e'',a'',a''',e'}_{\mathbf{p}_1'+\mathbf{q}',\mathbf{k}',\mathbf{k}'+\mathbf{q}',\mathbf{p}_1'} s(1, 1', \mathbf{k}, \mathbf{q}, a, a', \underline{t}_1, \mathbf{k}', \mathbf{q}', a'', a''', \underline{t}_1') \Big|^{\mathbf{p}_1-\mathbf{q},\bar{e}}_{\mathbf{p}_1'+\mathbf{q}',e''} \right\} \Bigg) \Bigg\}. \tag{A41}$$

Equation (A40) is not a full Dyson equation, since only the free exciton Green function $K_0(2, 1')$ appears on the rhs. It rather represents the first skeleton diagram of an expansion of the full exciton Green function with respect to M. As discussed in Ref. [34], it is meaningful to interpret M as a self-energy and upgrade $K_0(2, 1')$ to $K(2, 1')$. Indeed, it turns out that the four-particle Green functions can be factorized into two-particle Green functions such that the GW self-energy obtained from functional derivatives is reproduced. For example, the first four-particle term in Eq. (A41) can be rewritten as

$$\sum_{\mathbf{k},\mathbf{q},a,a'} \sum_{\mathbf{k}',\mathbf{q}',a'',a'''} \sum_{\bar{h}} \sum_{h''} s_a s_{a''} V^{h,a,a',\bar{h}}_{\mathbf{k}_1,\mathbf{k},\mathbf{k}+\mathbf{q},\mathbf{k}_1-\mathbf{q}} V^{h'',a'',a''',h'}_{\mathbf{k}_1'+\mathbf{q}',\mathbf{k}',\mathbf{k}'+\mathbf{q}',\mathbf{k}_1'} s(1, 1', \mathbf{k}, \mathbf{q}, a, a', \underline{t}_1, \mathbf{k}', \mathbf{q}', a'', a''', \underline{t}_1') \Big|^{\mathbf{k}_1-\mathbf{q},\bar{h}}_{\mathbf{k}_1'+\mathbf{q}',h''}$$

$$= \frac{1}{i\hbar} \sum_{\mathbf{k},\mathbf{q},a,a'} \sum_{\mathbf{k}',\mathbf{q}',a'',a'''} \sum_{\bar{h}} \sum_{h''} s_a s_{a''} V^{h,a,a',\bar{h}}_{\mathbf{k}_1,\mathbf{k},\mathbf{k}+\mathbf{q},\mathbf{k}_1-\mathbf{q}} V^{h'',a'',a''',h'}_{\mathbf{k}_1'+\mathbf{q}',\mathbf{k}',\mathbf{k}'+\mathbf{q}',\mathbf{k}_1'}$$

$$\times \langle\!\langle a^\dagger_{\mathbf{k}}(\underline{t}_1^+) a'_{\mathbf{k}+\mathbf{q}}(\underline{t}_1) \bar{h}_{\mathbf{k}_1-\mathbf{q}}(\underline{t}_1) e_{\mathbf{p}_1}(\underline{t}_1) e'^\dagger_{\mathbf{p}_1'}(\underline{t}_1') h''^\dagger_{\mathbf{k}_1'+\mathbf{q}'}(\underline{t}_1') a''^\dagger_{\mathbf{k}'}(\underline{t}'^+_1) a'''_{\mathbf{k}'+\mathbf{q}'}(\underline{t}_1') \rangle\!\rangle_T$$

$$\approx \frac{1}{i\hbar} \sum_{\mathbf{k},\mathbf{q},a,a'} \sum_{\mathbf{k}',\mathbf{q}',a'',a'''} \sum_{\bar{h}} \sum_{h''} s_a s_{a''} V^{h,a,a',\bar{h}}_{\mathbf{k}_1,\mathbf{k},\mathbf{k}+\mathbf{q},\mathbf{k}_1-\mathbf{q}} V^{h'',a'',a''',h'}_{\mathbf{k}_1'+\mathbf{q}',\mathbf{k}',\mathbf{k}'+\mathbf{q}',\mathbf{k}_1'}$$

$$\times \langle\!\langle a^\dagger_{\mathbf{k}}(\underline{t}_1^+) a'_{\mathbf{k}+\mathbf{q}}(\underline{t}_1) a''^\dagger_{\mathbf{k}'}(\underline{t}'^+_1) a'''_{\mathbf{k}'+\mathbf{q}'}(\underline{t}_1') \rangle\!\rangle_T \langle\!\langle \bar{h}_{\mathbf{k}_1-\mathbf{q}}(\underline{t}_1) e_{\mathbf{p}_1}(\underline{t}_1) e'^\dagger_{\mathbf{p}_1'}(\underline{t}_1') h''^\dagger_{\mathbf{k}_1'+\mathbf{q}'}(\underline{t}_1') \rangle\!\rangle_T$$

$$= \frac{1}{i\hbar} \sum_{\mathbf{k},\mathbf{q},a,a'} \sum_{\mathbf{k}',\mathbf{q}',a'',a'''} \sum_{\bar{h}} \sum_{h''} V^{h,a,a',\bar{h}}_{\mathbf{k}_1,\mathbf{k},\mathbf{k}+\mathbf{q},\mathbf{k}_1-\mathbf{q}} V^{h'',a'',a''',h'}_{\mathbf{k}_1'+\mathbf{q}',\mathbf{k}',\mathbf{k}'+\mathbf{q}',\mathbf{k}_1'}$$

$$\times i\hbar L(\mathbf{k}'+\mathbf{q}', -\mathbf{q}', a'', a''', \underline{t}_1', \mathbf{k}+\mathbf{q}, -\mathbf{q}, a, a', \underline{t}_1) i\hbar K(1, 1') \Big|^{\mathbf{k}_1-\mathbf{q},\bar{h}}_{\mathbf{k}_1'+\mathbf{q}',h''}$$

$$\approx i\hbar \sum_{\mathbf{k},\mathbf{q},\mathbf{q}',a,a'} \sum_{\bar{h},h''} V^{h,a,a',\bar{h}}_{\mathbf{k}_1,\mathbf{k},\mathbf{k}+\mathbf{q},\mathbf{k}_1-\mathbf{q}} \left(\varepsilon^{-1}(\mathbf{k}_1', -\mathbf{q}', h'', h', \underline{t}'^+_1, \mathbf{k}+\mathbf{q}, \mathbf{q}, a, a', \underline{t}_1) \right.$$

$$\left. - n_1 \delta_{n_1, n_1'} \delta(t_1 - t_1') \delta_{\mathbf{k}_1',\mathbf{k}+\mathbf{q}} \delta_{\mathbf{q},-\mathbf{q}'} \delta_{h'',a} \delta_{h',a'} \right) K(1, 1') \Big|^{\mathbf{k}_1-\mathbf{q},\bar{h}}_{\mathbf{k}_1'+\mathbf{q}',h''}. \tag{A42}$$

In the fourth line, we use the definition (A26) of the density-density expectation value. In the fifth line, we replaced the latter by the inverse dielectric function according to Eq. (A25), neglecting the term quadratic in the carrier density. The first term in the fifth line reproduces the hole-hole interaction term in the GW self-energy (A33), while the second cancels the corresponding instantaneous (Fock-like) contribution. We, therefore, note that the four-particle terms in $M(1, 1')$ contain the retarded part of the excitonic GW self-energy, while any instantaneous Hartree- and Fock-type interaction are described by the r_0 terms. Unlike in Ref. [34], we keep the retarded part of the GW self-energy as it is and focus on instantaneous correction terms contained in r_0.

We evaluate the r_0 terms in Eq. (A41) with Eq. (A38) by replacing the general band summation over a and a' by electron and hole bands and bringing all terms to normal order. Neglecting all expectation values with four electron or hole operators, respectively, the resulting instantaneous exciton self-energy is given by

$$M^\delta(1,1') = n_1 \delta_{n_1,n_1'} \delta(t_1 - t_1') \Big(M^{\delta,(1)}(1,1') + M^{\delta,(2)}(1,1') + M^{\delta,(3)}(1,1') + M^{\delta,(4)}(1,1') \Big) \tag{A43}$$

with

$$
\begin{aligned}
M^{\delta,(1)}(1,1') = \sum_{\mathbf{k}} \Bigg\{ &\sum_{h'',h'''} V^{h,h'',h''',h'}_{\mathbf{k}_1,\mathbf{k},\mathbf{k}+\mathbf{k}_1-\mathbf{k}_1',\mathbf{k}_1'} \delta_{\mathbf{p}_1,\mathbf{p}_1'} \delta_{e,e'} \langle\!\langle h''^{\dagger}_{\mathbf{k}}(t_1) h'''_{\mathbf{k}+\mathbf{k}_1-\mathbf{k}_1'}(t_1) \rangle\!\rangle \\
&- \sum_{e'',e'''} V^{h,e'',e''',h'}_{\mathbf{k}_1,\mathbf{k},\mathbf{k}+\mathbf{k}_1-\mathbf{k}_1',\mathbf{k}_1'} \delta_{\mathbf{p}_1,\mathbf{p}_1'} \delta_{e,e'} \langle\!\langle e''^{\dagger}_{\mathbf{k}}(t_1) e'''_{\mathbf{k}+\mathbf{k}_1-\mathbf{k}_1'}(t_1) \rangle\!\rangle \\
&- \sum_{h'',h'''} V^{e,h'',h''',e'}_{\mathbf{p}_1,\mathbf{k},\mathbf{k}+\mathbf{p}_1-\mathbf{p}_1',\mathbf{p}_1'} \delta_{\mathbf{k}_1,\mathbf{k}_1'} \delta_{h,h'} \langle\!\langle h''^{\dagger}_{\mathbf{k}}(t_1) h'''_{\mathbf{k}+\mathbf{p}_1-\mathbf{p}_1'}(t_1) \rangle\!\rangle \\
&+ \sum_{e'',e'''} V^{e,e'',e''',e'}_{\mathbf{p}_1,\mathbf{k},\mathbf{k}+\mathbf{p}_1-\mathbf{p}_1',\mathbf{p}_1'} \delta_{\mathbf{k}_1,\mathbf{k}_1'} \delta_{h,h'} \langle\!\langle e''^{\dagger}_{\mathbf{k}}(t_1) e'''_{\mathbf{k}+\mathbf{p}_1-\mathbf{p}_1'}(t_1) \rangle\!\rangle \Bigg\},
\end{aligned}
\tag{A44}
$$

$$
\begin{aligned}
M^{\delta,(2)}(1,1') = -\sum_{\mathbf{k}} \Bigg\{ &\sum_{h'',h'''} V^{h,h'',h',h'''}_{\mathbf{k}_1,\mathbf{k},\mathbf{k}_1',\mathbf{k}+\mathbf{k}_1-\mathbf{k}_1'} \delta_{\mathbf{p}_1,\mathbf{p}_1'} \delta_{e,e'} \langle\!\langle h''^{\dagger}_{\mathbf{k}}(t_1) h'''_{\mathbf{k}+\mathbf{k}_1-\mathbf{k}_1'}(t_1) \rangle\!\rangle - \sum_{e''} V^{h,e'',e',h'}_{\mathbf{k}_1,\mathbf{k},\mathbf{p}_1',\mathbf{k}_1'} \delta_{\mathbf{k},\mathbf{p}_1'+\mathbf{k}_1'-\mathbf{k}_1} \langle\!\langle e''^{\dagger}_{\mathbf{k}}(t_1) e_{\mathbf{p}_1}(t_1) \rangle\!\rangle \\
&- \sum_{h''} V^{e,h'',h',e'}_{\mathbf{p}_1,\mathbf{k},\mathbf{k}_1',\mathbf{p}_1'} \delta_{\mathbf{k},\mathbf{k}_1'+\mathbf{p}_1'-\mathbf{p}_1} \langle\!\langle h''^{\dagger}_{\mathbf{k}}(t_1) h_{\mathbf{k}_1}(t_1) \rangle\!\rangle + \sum_{e'',e'''} V^{e,e'',e',e'''}_{\mathbf{p}_1,\mathbf{k},\mathbf{p}_1',\mathbf{k}+\mathbf{p}_1-\mathbf{p}_1'} \delta_{\mathbf{k}_1,\mathbf{k}_1'} \delta_{h,h'} \langle\!\langle e''^{\dagger}_{\mathbf{k}}(t_1) e'''_{\mathbf{k}+\mathbf{p}_1-\mathbf{p}_1'}(t_1) \rangle\!\rangle \Bigg\},
\end{aligned}
\tag{A45}
$$

$$
\begin{aligned}
M^{\delta,(3)}(1,1') = \sum_{\mathbf{q}} \Bigg\{ &\sum_{h'',h'''} V^{h,h'',h',h'''}_{\mathbf{k}_1,\mathbf{k}_1'-\mathbf{q},\mathbf{k}_1',\mathbf{k}_1-\mathbf{q}} \langle\!\langle h''^{\dagger}_{\mathbf{k}_1'-\mathbf{q}}(t_1) e'^{\dagger}_{\mathbf{p}_1'}(t_1) e_{\mathbf{p}_1}(t_1) h'''_{\mathbf{k}_1-\mathbf{q}}(t_1) \rangle\!\rangle \\
&- \sum_{e'',h'''} V^{h,e'',e',h'''}_{\mathbf{k}_1,\mathbf{p}_1'-\mathbf{q},\mathbf{p}_1',\mathbf{k}_1-\mathbf{q}} \langle\!\langle h'^{\dagger}_{\mathbf{k}_1'}(t_1) e''^{\dagger}_{\mathbf{p}_1'-\mathbf{q}}(t_1) e_{\mathbf{p}_1}(t_1) h'''_{\mathbf{k}_1-\mathbf{q}}(t_1) \rangle\!\rangle \\
&- \sum_{h'',e'''} V^{e,h'',h',e'''}_{\mathbf{p}_1,\mathbf{k}_1'-\mathbf{q},\mathbf{k}_1',\mathbf{p}_1-\mathbf{q}} \langle\!\langle h''^{\dagger}_{\mathbf{k}_1'-\mathbf{q}}(t_1) e'^{\dagger}_{\mathbf{p}_1'}(t_1) e'''_{\mathbf{p}_1-\mathbf{q}}(t_1) h_{\mathbf{k}_1}(t_1) \rangle\!\rangle \\
&+ \sum_{e'',e'''} V^{e,e'',e',e'''}_{\mathbf{p}_1,\mathbf{p}_1'-\mathbf{q},\mathbf{p}_1',\mathbf{p}_1-\mathbf{q}} \langle\!\langle h'^{\dagger}_{\mathbf{k}_1'}(t_1) e''^{\dagger}_{\mathbf{p}_1'-\mathbf{q}}(t_1) e'''_{\mathbf{p}_1-\mathbf{q}}(t_1) h_{\mathbf{k}_1}(t_1) \rangle\!\rangle \Bigg\},
\end{aligned}
\tag{A46}
$$

and

$$
\begin{aligned}
M^{\delta,(4)}(1,1') = -\sum_{\mathbf{q}} \Bigg\{ &\sum_{h'',h'''} V^{h,h'',h''',h''}_{\mathbf{k}_1,\mathbf{k}_1'-\mathbf{q},\mathbf{k}_1-\mathbf{q},\mathbf{k}_1'} \langle\!\langle h''^{\dagger}_{\mathbf{k}_1'-\mathbf{q}}(t_1) e'^{\dagger}_{\mathbf{p}_1'}(t_1) e_{\mathbf{p}_1}(t_1) h'''_{\mathbf{k}_1-\mathbf{q}}(t_1) \rangle\!\rangle \\
&- \sum_{\mathbf{k},e'',e''',h'''} V^{h,e'',e''',h'''}_{\mathbf{k}_1,\mathbf{k},\mathbf{k}+\mathbf{q},\mathbf{k}_1-\mathbf{q}} \delta_{\mathbf{p}_1,\mathbf{p}_1'} \delta_{e,e'} \langle\!\langle h'^{\dagger}_{\mathbf{k}_1'}(t_1) e''^{\dagger}_{\mathbf{k}}(t_1) e'''_{\mathbf{k}+\mathbf{q}}(t_1) h'''_{\mathbf{k}_1-\mathbf{q}}(t_1) \rangle\!\rangle \\
&- \sum_{\mathbf{k},h'',h''',e'''} V^{e,h'',h''',e'''}_{\mathbf{p}_1,\mathbf{k},\mathbf{k}+\mathbf{q},\mathbf{p}_1-\mathbf{q}} \delta_{\mathbf{k}_1,\mathbf{k}_1'} \delta_{h,h'} \langle\!\langle h''^{\dagger}_{\mathbf{k}}(t_1) e'^{\dagger}_{\mathbf{p}_1'}(t_1) e'''_{\mathbf{p}_1-\mathbf{q}}(t_1) h'''_{\mathbf{k}+\mathbf{q}}(t_1) \rangle\!\rangle \\
&+ \sum_{e'',e'''} V^{e,e'',e''',e'}_{\mathbf{p}_1,\mathbf{p}_1'-\mathbf{q},\mathbf{p}_1-\mathbf{q},\mathbf{p}_1'} \langle\!\langle h'^{\dagger}_{\mathbf{k}_1'}(t_1) e''^{\dagger}_{\mathbf{p}_1'-\mathbf{q}}(t_1) e'''_{\mathbf{p}_1-\mathbf{q}}(t_1) h_{\mathbf{k}_1}(t_1) \rangle\!\rangle \Bigg\}.
\end{aligned}
\tag{A47}
$$

The terms $M^{\delta,(1)}$ and $M^{\delta,(2)}$, being proportional to electron and hole occupancies, correspond to the single-particle Hartree and Fock self-energies, respectively. As discussed in detail in Ref. [34], the single-particle occupancies can be approximately projected to the phase space of excitons using the relations

$$h_{\mathbf{k}}^{\dagger} h'_{\mathbf{k}'} \approx \sum_{\mathbf{p},e} e_{\mathbf{p}}^{\dagger} h_{\mathbf{k}}^{\dagger} h'_{\mathbf{k}'} e_{\mathbf{p}}, \quad e_{\mathbf{p}}^{\dagger} e'_{\mathbf{p}'} \approx \sum_{\mathbf{k},h} e_{\mathbf{p}}^{\dagger} h_{\mathbf{k}}^{\dagger} h_{\mathbf{k}} e'_{\mathbf{p}'}. \quad \text{(A48)}$$

A similar projection technique has also been used in Refs. [18,72]. The resulting four-particle expectation values, along with the corresponding terms in $M^{\delta,(3)}$ and $M^{\delta,(4)}$, can be interpreted as exciton Green functions evaluated on the time diagonal according to

$$i\hbar K(1,1')\Big|_{\underline{t}'_1 = \underline{t}_1^+} = \langle\!\langle h_{\mathbf{k}'_1}^{\dagger}(\underline{t}_1^+) e'^{\dagger}_{\mathbf{p}'_1}(\underline{t}_1^+) e_{\mathbf{p}_1}(\underline{t}_1) h_{\mathbf{k}_1}(\underline{t}_1) \rangle\!\rangle.$$

$$\text{(A49)}$$

We note that the above projection in phase space assumes that any photoexcited electron or hole is part of a bound

exciton, while no higher-order complexes such as biexcitons contribute beyond a pure factorization in pairs of excitons. This is an assumption that becomes more accurate for lower densities. It is consistent with a treatment of renormalization effects by means of a Dyson-type equation for the exciton Green function with a self-energy formulated solely in terms of excitons [upgraded Eq. (A40)]. The Dyson-type equation establishes a self-consistency within the exciton gas but does not introduce any higher-order complexes.

4. Real-time self-energy in the exciton representation

We now switch to an exciton representation of the instantaneous self-energy by introducing

$$G(\nu_1, \mathbf{Q}_1, \underline{t}_1, \nu'_1, \mathbf{Q}'_1, \underline{t}'_1) = \sum_{\mathbf{k}_1, \mathbf{p}_1, \mathbf{k}'_1, \mathbf{p}'_1, e, h, e', h'} \Phi^*_{\nu_1, \mathbf{Q}_1}(e, \mathbf{p}_1, h, \mathbf{k}_1) K(1,1') \Phi_{\nu'_1, \mathbf{Q}'_1}(e', \mathbf{p}'_1, h', \mathbf{k}'_1) \quad \text{(A50)}$$

with exciton wave functions as solutions to the Bethe-Salpeter equation that corresponds to the effective exciton Hamiltonian (A18):

$$(\varepsilon^e_{\mathbf{p}} + \varepsilon^h_{\mathbf{k}}) \Phi_{\nu, \mathbf{Q}}(e, \mathbf{p}, h, \mathbf{k}) - \sum_{\mathbf{q}, h', e'} V^{e,h,h',e'}_{\mathbf{p},\mathbf{k},\mathbf{k}+\mathbf{q},\mathbf{p}-\mathbf{q}} \Phi_{\nu, \mathbf{Q}}(e', \mathbf{p} - \mathbf{q}, h', \mathbf{k} + \mathbf{q}) = E_{\nu, \mathbf{Q}} \Phi_{\nu, \mathbf{Q}}(e, \mathbf{p}, h, \mathbf{k}). \quad \text{(A51)}$$

The quantum number of the relative electron-hole motion is denoted by ν, while the total exciton momentum is $\mathbf{Q} = \mathbf{k} + \mathbf{p}$. Exciton energies are denoted by $E_{\nu,\mathbf{Q}}$. Since the wave functions form a basis of the electron-hole-pair Hilbert space, the exciton representation can be inverted:

$$K(1,1') = \sum_{\nu_1, \nu'_1, \mathbf{Q}_1, \mathbf{Q}'_1} \Phi_{\nu_1, \mathbf{Q}_1}(e, \mathbf{p}_1, h, \mathbf{k}_1) G(\nu_1, \mathbf{Q}_1, \underline{t}_1, \nu'_1, \mathbf{Q}'_1, \underline{t}'_1) \Phi^*_{\nu'_1, \mathbf{Q}'_1}(e', \mathbf{p}'_1, h', \mathbf{k}'_1). \quad \text{(A52)}$$

We obtain the exciton Hartree self-energy from Eq. (A44) and the first and fourth terms in Eq. (A45) as

$$\Sigma^{\mathrm{H}}(\nu_1, \mathbf{Q}_1, \underline{t}_1, \nu'_1, \mathbf{Q}'_1, \underline{t}'_1) = i\hbar n_1 \delta_{n_1, n'_1} \delta(t_1 - t'_1) \sum_{\nu_2, \nu'_2, \mathbf{Q}_2, \mathbf{Q}'_2} \tilde{V}^{\nu_1, \nu'_2, \nu_2, \nu'_1}_{\mathbf{Q}_1, \mathbf{Q}'_2, \mathbf{Q}_2, \mathbf{Q}'_1} G(\nu_2, \mathbf{Q}_2, \underline{t}_1, \nu'_2, \mathbf{Q}'_2, \underline{t}_1) \quad \text{(A53)}$$

with the effective exciton-exciton interaction matrix elements

$$\tilde{V}^{\nu_1, \nu_2, \nu_3, \nu_4}_{\mathbf{Q}_1, \mathbf{Q}_2, \mathbf{Q}_3, \mathbf{Q}_4} = \tilde{V}^{\nu_1, \nu_2, \nu_3, \nu_4}_{\mathbf{Q}_1, \mathbf{Q}_2, \mathbf{Q}=\mathbf{Q}_3-\mathbf{Q}_2}$$

$$= \sum_{\mathbf{k}_1, \mathbf{k}_2, h_1, h_2, e_1, e_2} \Phi^*_{\nu_1, \mathbf{Q}_1}(e_1, h_1, \mathbf{k}_1) \Phi_{\nu_3, \mathbf{Q}_2+\mathbf{Q}}(e_2, h_2, \mathbf{k}_2) \Bigg\{ \sum_{\bar{e}} \Phi^*_{\nu_2, \mathbf{Q}_2}(\bar{e}, h_2, \mathbf{k}_2)$$

$$\times \Bigg(\sum_{e'} V^{e_1, \bar{e}, e_2, e'}_{\mathbf{Q}_1-\mathbf{k}_1, \mathbf{Q}_2-\mathbf{k}_2, \mathbf{Q}_2-\mathbf{k}_2+\mathbf{Q}, \mathbf{Q}_1-\mathbf{k}_1-\mathbf{Q}} \Phi_{\nu_4, \mathbf{Q}_1-\mathbf{Q}}(e', h_1, \mathbf{k}_1)$$

$$- \sum_{e'} V^{e_1, \bar{e}, e', e_2}_{\mathbf{Q}_1-\mathbf{k}_1, \mathbf{Q}_2-\mathbf{k}_2, \mathbf{Q}_1-\mathbf{k}_1-\mathbf{Q}, \mathbf{Q}_2-\mathbf{k}_2+\mathbf{Q}} \Phi_{\nu_4, \mathbf{Q}_1-\mathbf{Q}}(e', h_1, \mathbf{k}_1) - \sum_{h'} V^{h_1, \bar{e}, e_2, h'}_{\mathbf{k}_1, \mathbf{Q}_2-\mathbf{k}_2, \mathbf{Q}_2-\mathbf{k}_2+\mathbf{Q}, \mathbf{k}_1-\mathbf{Q}} \Phi_{\nu_4, \mathbf{Q}_1-\mathbf{Q}}(e_1, h', \mathbf{k}_1-\mathbf{Q}) \Bigg)$$

$$+ \sum_{\bar{h}} \Phi^*_{\nu_2, \mathbf{Q}_2}(e_2, \bar{h}, \mathbf{k}_2-\mathbf{Q}) \Bigg(\sum_{h'} V^{h_1, \bar{h}, h_2, h'}_{\mathbf{k}_1, \mathbf{k}_2-\mathbf{Q}, \mathbf{k}_2, \mathbf{k}_1-\mathbf{Q}} \Phi_{\nu_4, \mathbf{Q}_1-\mathbf{Q}}(e_1, h', \mathbf{k}_1-\mathbf{Q})$$

$$- \sum_{h'} V^{h_1, \bar{h}, h', h_2}_{\mathbf{k}_1, \mathbf{k}_2-\mathbf{Q}, \mathbf{k}_1-\mathbf{Q}, \mathbf{k}_2} \Phi_{\nu_4, \mathbf{Q}_1-\mathbf{Q}}(e_1, h', \mathbf{k}_1-\mathbf{Q}) - \sum_{e'} V^{e_1, \bar{h}, h_2, e'}_{\mathbf{Q}_1-\mathbf{k}_1, \mathbf{k}_2-\mathbf{Q}, \mathbf{k}_2, \mathbf{Q}_1-\mathbf{k}_1-\mathbf{Q}} \Phi_{\nu_4, \mathbf{Q}_1-\mathbf{Q}}(e', h_1, \mathbf{k}_1) \Bigg) \Bigg\}$$

$$= \tilde{V}^{(\mathrm{D}),\nu_1,\nu_2,\nu_3,\nu_4}_{\mathbf{Q}_1, \mathbf{Q}_2, \mathbf{Q}=\mathbf{Q}_3-\mathbf{Q}_2} - \tilde{V}^{(\mathrm{X}),\nu_1,\nu_2,\nu_3,\nu_4}_{\mathbf{Q}_1, \mathbf{Q}_2, \mathbf{Q}=\mathbf{Q}_3-\mathbf{Q}_2}. \quad \text{(A54)}$$

Note that we make use of the momentum conservation relation $\mathbf{p} = \mathbf{Q} - \mathbf{k}$ implied in the exciton wave functions to eliminate electron momenta. Terms number 1, 3, 4, and 6 stem from the single-particle Hartree term and correspond to the semiclassical dipolar Coulomb interaction between excitons [27], which is described by $\tilde{V}^{(D)}$. We find two repulsive and two attractive contributions caused by the opposite charge of electrons and holes. Terms number 2 and 5, however, are nonclassical terms due to the fermionic nature of the exciton constituents: These fermionic correction terms describe the exchange of either an electron or a hole between two excitons leading to an attractive interaction proportional to $\tilde{V}^{(X)}$. Notably, besides the sign the only difference between "direct" and "exchange" terms inside the effective matrix element is the swap of two states in the elementary Coulomb matrix element.

In a similar way, an exciton Fock self-energy is obtained from Eq. (A46) as well as the first and fourth terms in Eq. (A47):

$$\Sigma^{F}(\nu_1, \mathbf{Q}_1, \underline{t}_1, \nu_1', \mathbf{Q}_1', \underline{t}_1') = i\hbar n_1 \delta_{n_1, n_1'} \delta(t_1 - t_1') \sum_{\nu_2, \nu_2', \mathbf{Q}_2, \mathbf{Q}_2'} \tilde{V}^{\nu_1, \nu_2', \nu_1', \nu_2}_{\mathbf{Q}_1, \mathbf{Q}_2', \mathbf{Q}_1', \mathbf{Q}_2} G(\nu_2, \mathbf{Q}_2, \underline{t}_1, \nu_2', \mathbf{Q}_2', \underline{t}_1). \tag{A55}$$

The exciton Fock self-energy can be interpreted as resulting from the bosonic exchange of two excitons, with only two states in the effective matrix element swapped with respect to the exciton Hartree term. As the latter, the Fock term contains fermionic exchange terms.

The remaining four terms of the instantaneous self-energy, which are the second and third terms in Eqs. (A45) and (A47), respectively, can be grouped together similar to the exciton Hartree and Fock self-energies:

$$\Sigma^{PB}(\nu_1, \mathbf{Q}_1, \underline{t}_1, \nu_1', \mathbf{Q}_1', \underline{t}_1') = i\hbar n_1 \delta_{n_1, n_1'} \delta(t_1 - t_1') \sum_{\nu_2, \nu_2', \mathbf{Q}_2, \mathbf{Q}_2'} \left(\tilde{V}^{PB, \nu_1, \nu_2', \nu_2, \nu_1'}_{\mathbf{Q}_1, \mathbf{Q}_2', \mathbf{Q}_2, \mathbf{Q}_1'} + \tilde{V}^{PB, \nu_1, \nu_2', \nu_1', \nu_2}_{\mathbf{Q}_1, \mathbf{Q}_2', \mathbf{Q}_1', \mathbf{Q}_2} \right) G(\nu_2, \mathbf{Q}_2, \underline{t}_1, \nu_2', \mathbf{Q}_2', \underline{t}_1). \tag{A56}$$

We introduce new effective matrix elements

$$
\begin{aligned}
\tilde{V}^{PB, \nu_1, \nu_2, \nu_3, \nu_4}_{\mathbf{Q}_1, \mathbf{Q}_2, \mathbf{Q}_3, \mathbf{Q}_4} &= \tilde{V}^{PB, \nu_1, \nu_2, \nu_3, \nu_4}_{\mathbf{Q}_1, \mathbf{Q}_2, \bar{\mathbf{Q}} = \mathbf{Q}_4 - \mathbf{Q}_2} \\
&= \sum_{\mathbf{k}_1, \mathbf{k}_2, h_1, h_2, e_1, e_2} \Phi^{*}_{\nu_1, \mathbf{Q}_1}(e_1, h_1, \mathbf{k}_1) \\
&\quad \times \Bigg\{ \Phi_{\nu_4, \mathbf{Q}_2 + \bar{\mathbf{Q}}}(e_2, h_2, \mathbf{k}_2) \sum_{\bar{h}, e''} V^{h_1, e'', e_2, h_2}_{\mathbf{k}_1, \mathbf{Q}_2 + \bar{\mathbf{Q}} - \mathbf{k}_1, \mathbf{Q}_2 + \bar{\mathbf{Q}} - \mathbf{k}_2, \mathbf{k}_2} \Phi_{\nu_3, \mathbf{Q}_1 - \bar{\mathbf{Q}}}(e_1, \bar{h}, \mathbf{k}_1 - \bar{\mathbf{Q}}) \Phi^{*}_{\nu_2, \mathbf{Q}_2}(e'', \bar{h}, \mathbf{k}_1 - \bar{\mathbf{Q}}) \\
&\quad + \Phi_{\nu_3, \mathbf{Q}_1 - \bar{\mathbf{Q}}}(e_2, h_2, \mathbf{k}_2 - \bar{\mathbf{Q}}) \sum_{\bar{e}, h''} V^{h'', e_1, e_2, h_2}_{\mathbf{k}_1 - \bar{\mathbf{Q}}, \mathbf{Q}_1 - \mathbf{k}_1, \mathbf{Q}_1 - \mathbf{k}_2, \mathbf{k}_2 - \bar{\mathbf{Q}}} \Phi_{\nu_4, \mathbf{Q}_2 + \bar{\mathbf{Q}}}(\bar{e}, h_1, \mathbf{k}_1) \Phi^{*}_{\nu_2, \mathbf{Q}_2}(\bar{e}, h'', \mathbf{k}_1 - \bar{\mathbf{Q}}) \Bigg\}. \tag{A57}
\end{aligned}
$$

The self-energy contribution (A56) appears on the same level as the Hartree-Fock energy renormalizations, is proportional to electron-hole interaction matrix elements, and has the positive sign of a repulsive interaction. It is, therefore, plausible to attribute the self-energy to Pauli blocking caused by phase-space filling from the fermionic constituents. In a Bethe-Salpeter or Wannier equation for the exciton, phase-space filling appears as a prefactor similar to Eq. (A15) of the electron-hole term, thereby reducing the exciton binding energy [42]. Expanding the densitylike terms in the phase-space filling factor according to Eq. (A48) and adding the corresponding bosonic exchange term, Σ^{PB} can be derived. We note that, unlike the fermionic exchange corrections in Σ^{H} and Σ^{F}, Σ^{PB} cannot simply be obtained by swapping two states in a Coulomb matrix element. Both the fermionic correction terms and the Pauli-blocking terms are beyond the RPA self-energy derived in the previous subsection via functional derivative technique.

We now bring the retarded part of the exciton GW self-energy to a form similar to the above exciton Hartree and Fock self-energies. Starting from Eq. (A42), we derive an expression that contains the fully screened Coulomb interaction W. Based on the arrangement of operators in the definition (A25), the elements of the dielectric matrix can be identified as

$$
\begin{aligned}
\varepsilon^{-1}(\mathbf{k}_2 + \mathbf{q}_2, \mathbf{q}_2, a_2, a_2', \underline{t}_2, \mathbf{k} + \mathbf{q}, \mathbf{q}, a, a', \underline{t}_1) &= \langle \psi^{a_2}_{\mathbf{k}_2} | \langle \psi^{a'}_{\mathbf{k}+\mathbf{q}} | \varepsilon^{-1}(\mathbf{r}, \mathbf{r}', \underline{t}_2, \underline{t}_1) | \psi^{a}_{\mathbf{k}} \rangle | \psi^{a_2'}_{\mathbf{k}_2 + \mathbf{q}_2} \rangle \\
&\approx \varepsilon^{-1, a_2, a', a, a_2'}_{\mathbf{k}_2, \mathbf{k}+\mathbf{q}, \mathbf{k}, \mathbf{k}_2 + \mathbf{q}_2}(\underline{t}_2, \underline{t}_1) \delta_{\mathbf{q}, \mathbf{q}_2} \delta_{\mathbf{k}, \mathbf{k}_2}, \tag{A58}
\end{aligned}
$$

in analogy to Coulomb matrix elements. The first Kronecker delta takes momentum conservation into account, while the second is an additional approximation. Expanding the dielectric and Coulomb matrix elements in terms of Wannier functions and making use of the completeness of Bloch states, we find

$$
i\hbar \sum_{\mathbf{k},\mathbf{q},\mathbf{q}',a,a'} \sum_{\bar{h},h''} V^{h,a,a',\bar{h}}_{\mathbf{k}_1,\mathbf{k},\mathbf{k}+\mathbf{q},\mathbf{k}_1-\mathbf{q}} \varepsilon^{-1}(\mathbf{k}'_1, -\mathbf{q}', h'', h', \underline{t}'^+_1, \mathbf{k}+\mathbf{q}, \mathbf{q}, a, a', \underline{t}_1) K(1,1') \Big|^{\mathbf{k}_1-\mathbf{q},\bar{h}}_{\mathbf{k}'_1+\mathbf{q}',h''}
$$

$$
= i\hbar \sum_{\mathbf{q},a,a'} \sum_{\bar{h},h''} V^{h,a,a',\bar{h}}_{\mathbf{k}_1,\mathbf{k}'_1-\mathbf{q},\mathbf{k}'_1,\mathbf{k}_1-\mathbf{q}} \varepsilon^{-1,h'',a',a,h'}_{\mathbf{k}'_1-\mathbf{q},\mathbf{k}'_1,\mathbf{k}'_1-\mathbf{q},\mathbf{k}'_1}(\underline{t}'^+_1, \underline{t}_1) K(1,1') \Big|^{\mathbf{k}_1-\mathbf{q},\bar{h}}_{\mathbf{k}'_1-\mathbf{q},h''}
$$

$$
= i\hbar \sum_{\mathbf{q}} \sum_{\bar{h},h''} \sum_{\alpha,\alpha'} (c^{h''}_{\alpha',\mathbf{k}'_1-\mathbf{q}})^* (c^h_{\alpha,\mathbf{k}_1})^* W^{\alpha'\alpha}_{-\mathbf{q}}(\underline{t}'^+_1, \underline{t}_1) c^{\bar{h}}_{\alpha,\mathbf{k}_1-\mathbf{q}} c^{h'}_{\alpha',\mathbf{k}'_1} K(1,1') \Big|^{\mathbf{k}_1-\mathbf{q},\bar{h}}_{\mathbf{k}'_1-\mathbf{q},h''}
$$

$$
= i\hbar \sum_{\mathbf{q}} \sum_{\bar{h},h''} W^{h'',h,\bar{h},h'}_{\mathbf{k}'_1-\mathbf{q},\mathbf{k}_1,\mathbf{k}_1-\mathbf{q},\mathbf{k}'_1}(\underline{t}'^+_1, \underline{t}_1) K(1,1') \Big|^{\mathbf{k}_1-\mathbf{q},\bar{h}}_{\mathbf{k}'_1-\mathbf{q},h''} \tag{A59}
$$

with the fully screened Coulomb matrix

$$
W^{\alpha\beta}_{\mathbf{q}}(\underline{t},\underline{t}') = \sum_{\gamma} \varepsilon^{-1,\alpha\gamma}_{\mathbf{q}}(\underline{t},\underline{t}') V^{\gamma\beta}_{\mathbf{q}}. \tag{A60}
$$

Analogous calculations are carried out for the three remaining four-particle terms in Eq. (A41). Then, we arrive at the exciton *GW* self-energy:

$$
\Sigma^{GW}(\nu_1, \mathbf{Q}_1, \underline{t}_1, \nu'_1, \mathbf{Q}'_1, \underline{t}'_1) = i\hbar \sum_{\nu_2,\nu'_2,\mathbf{Q}_2,\mathbf{Q}'_2} \tilde{W}^{\nu_1,\nu'_2,\nu'_1,\nu_2}_{\mathbf{Q}_1,\mathbf{Q}'_2,\mathbf{Q}'_1,\mathbf{Q}_2}(\underline{t}'_1, \underline{t}_1) G(\nu_2, \mathbf{Q}_2, \underline{t}_1, \nu'_2, \mathbf{Q}'_2, \underline{t}'_1) \tag{A61}
$$

with the effective matrix element

$$
\tilde{W}^{\nu_1,\nu_2,\nu_3,\nu_4}_{\mathbf{Q}_1,\mathbf{Q}_2,\mathbf{Q}=\mathbf{Q}_3-\mathbf{Q}_2}(\underline{t}'_1, \underline{t}_1) = \sum_{\mathbf{k}_1,\mathbf{k}_2,h_1,h_2,e_1,e_2} \Phi^*_{\nu_1,\mathbf{Q}_1}(e_1, h_1, \mathbf{k}_1) \Phi_{\nu_3,\mathbf{Q}_2+\mathbf{Q}}(e_2, h_2, \mathbf{k}_2)
$$

$$
\times \Bigg\{ \sum_{\bar{e}} \Phi^*_{\nu_2,\mathbf{Q}_2}(\bar{e}, h_2, \mathbf{k}_2) \Bigg(\sum_{e'} W^{\bar{e},e_1,e',e_2}_{\mathbf{Q}_2-\mathbf{k}_2,\mathbf{Q}_1-\mathbf{k}_1,\mathbf{Q}_1-\mathbf{k}_1-\mathbf{Q},\mathbf{Q}_2-\mathbf{k}_2+\mathbf{Q}}(\underline{t}'_1, \underline{t}_1) \Phi_{\nu_4,\mathbf{Q}_1-\mathbf{Q}}(e', h_1, \mathbf{k}_1)
$$

$$
- \sum_{h'} W^{\bar{e},h_1,h',e_2}_{\mathbf{Q}_2-\mathbf{k}_2,\mathbf{k}_1,\mathbf{k}_1-\mathbf{Q},\mathbf{Q}_2-\mathbf{k}_2+\mathbf{Q}}(\underline{t}'_1, \underline{t}_1) \Phi_{\nu_4,\mathbf{Q}_1-\mathbf{Q}}(e_1, h', \mathbf{k}_1 - \mathbf{Q}) \Bigg)
$$

$$
+ \sum_{\bar{h}} \Phi^*_{\nu_2,\mathbf{Q}_2}(e_2, \bar{h}, \mathbf{k}_2 - \mathbf{Q}) \Bigg(\sum_{h'} W^{\bar{h},h_1,h',h_2}_{\mathbf{k}_2-\mathbf{Q},\mathbf{k}_1,\mathbf{k}_1-\mathbf{Q},\mathbf{k}_2}(\underline{t}'_1, \underline{t}_1) \Phi_{\nu_4,\mathbf{Q}_1-\mathbf{Q}}(e_1, h', \mathbf{k}_1 - \mathbf{Q})
$$

$$
- \sum_{e'} W^{\bar{h},e_1,e',h_2}_{\mathbf{k}_2-\mathbf{Q}_2,\mathbf{Q}_1-\mathbf{k}_1,\mathbf{Q}_1-\mathbf{k}_1-\mathbf{Q},\mathbf{k}_2}(\underline{t}'_1, \underline{t}_1) \Phi_{\nu_4,\mathbf{Q}_1-\mathbf{Q}}(e', h_1, \mathbf{k}_1) \Bigg) \Bigg\}. \tag{A62}
$$

In summary, we obtain a Dyson-type equation for the exciton Green function by upgrading Eq. (A40):

$$
\int_{\mathcal{C}} d\underline{t}_2 \sum_{\mathbf{k}_2,\mathbf{p}_2,h_2,e_2} K^{-1}_0(1,2) K(2,1') = n_1 \delta_{n_1,n'_1} \delta(t_1 - t'_1) F(1,1') + \int_{\mathcal{C}} d\underline{t}_2 \sum_{\mathbf{k}_2,\mathbf{p}_2,h_2,e_2} M(1,2) K(2,1'). \tag{A63}
$$

The exciton self-energy $M(1,2)$ contains Hartree- and Fock-type contributions including fermionic corrections and a Pauli-blocking term as well as an RPA-type correlation term stemming from the factorization of four-particle Green functions.

Consistent with the derivation of the RPA vertex function in Eqs. (A31) and (A32), we drop the densitylike terms in $F(1, 1')$. Then, using the Bethe-Salpeter equation (A51), Dyson's equation can be expressed in the exciton representation:

$$\int_{\mathcal{C}} d\underline{t_2} \sum_{\nu_2, \mathbf{Q}_2} \left\{ \left(i\hbar \frac{\partial}{\partial t_1} - E_{\nu_1, \mathbf{Q}_1} \right) \delta_{\nu_1, \nu_2} \delta_{\mathbf{Q}_1, \mathbf{Q}_2} n_1 \delta_{n_1, n_2} \delta(t_1 - t_2) \right.$$

$$\left. - \Sigma^{\mathrm{H}}(\nu_1, \mathbf{Q}_1, \underline{t_1}, \nu_2, \mathbf{Q}_2, \underline{t_2}) - \Sigma^{\mathrm{F}}(\nu_1, \mathbf{Q}_1, \underline{t_1}, \nu_2, \mathbf{Q}_2, \underline{t_2}) - \Sigma^{\mathrm{PB}}(\nu_1, \mathbf{Q}_1, \underline{t_1}, \nu_2, \mathbf{Q}_2, \underline{t_2}) \right\} G(\nu_2, \mathbf{Q}_2, \underline{t_2}, \nu_1', \mathbf{Q}_1', \underline{t_1'})$$

$$= n_1 \delta_{n_1, n_1'} \delta(t_1 - t_1') \delta_{\nu_1, \nu_1'} \delta_{\mathbf{Q}_1, \mathbf{Q}_1'}$$

$$+ \int_{\mathcal{C}} d\underline{t_2} \sum_{\nu_2, \mathbf{Q}_2} \left(\Sigma^{GW}(\nu_1, \mathbf{Q}_1, \underline{t_1}, \nu_2, \mathbf{Q}_2, \underline{t_2}) - \Sigma^{GW, \delta}(\nu_1, \mathbf{Q}_1, \underline{t_1}, \nu_2, \mathbf{Q}_2, \underline{t_2}) \right) G(\nu_2, \mathbf{Q}_2, \underline{t_2}, \nu_1', \mathbf{Q}_1', \underline{t_1'}). \tag{A64}$$

Here, $\Sigma^{GW, \delta}$ denotes the instantaneous part of the exciton-GW self-energy emerging from the factorization of four-particle Green functions according to Eq. (A42). As described in Refs. [34,40,73], we transform Dyson's equation to physical times by unfolding the Keldysh contour ($\int_{\mathcal{C}} d\underline{t_2} = \sum_{n_2} \int_{-\infty}^{\infty} dt_2$), dropping the external potential and using the Langreth-Wilkins theorems. In close analogy to single-particle Green functions, we introduce greater and lesser Green functions

$$g^>(\nu_1, \mathbf{Q}_1, t_1, \nu_1', \mathbf{Q}_1', t_1') = G^{n_1 = -, n_1' = +}(\nu_1, \mathbf{Q}_1, t_1, \nu_1', \mathbf{Q}_1', t_1'),$$

$$g^<(\nu_1, \mathbf{Q}_1, t_1, \nu_1', \mathbf{Q}_1', t_1') = G^{n_1 = +, n_1' = -}(\nu_1, \mathbf{Q}_1, t_1, \nu_1', \mathbf{Q}_1', t_1') \tag{A65}$$

and retarded Green functions

$$g^{\mathrm{ret}}(\nu_1, \mathbf{Q}_1, t_1, \nu_1', \mathbf{Q}_1', t_1') = \theta(t_1 - t_1') \left(g^>(\nu_1, \mathbf{Q}_1, t_1, \nu_1', \mathbf{Q}_1', t_1') - g^<(\nu_1, \mathbf{Q}_1, t_1, \nu_1', \mathbf{Q}_1', t_1') \right). \tag{A66}$$

Retarded self-energies additionally contain an instantaneous contribution:

$$\Sigma^{\mathrm{ret}}(\nu_1, \mathbf{Q}_1, t_1, \nu_1', \mathbf{Q}_1', t_1') = \Sigma^{\delta}(\nu_1, \mathbf{Q}_1, t_1, \nu_1', \mathbf{Q}_1', t_1') + \theta(t_1 - t_1') \left(\Sigma^>(\nu_1, \mathbf{Q}_1, t_1, \nu_1', \mathbf{Q}_1', t_1') - \Sigma^<(\nu_1, \mathbf{Q}_1, t_1, \nu_1', \mathbf{Q}_1', t_1') \right). \tag{A67}$$

In the following, we assume that Green functions and self-energies are diagonal in the exciton representation. Equal-time Green functions, which appear in the instantaneous self-energy, correspond to $g^<$ functions, consistent with the replacement (A49). We further assume that the exciton gas is in a quasiequilibrium state, where $g^<$ is a time-independent distribution function. We again discard Pauli-blocking nonlinearities by describing excitons as ideal bosons, which implies

$$i\hbar g^<(\nu_1, \mathbf{Q}_1) = N_{\nu_1, \mathbf{Q}_1}^{\mathrm{X}} = \left[\exp\left(\frac{E_{\nu_1, \mathbf{Q}_1} - \mu_{\mathrm{X}}}{k_{\mathrm{B}} T} \right) - 1 \right]^{-1} \tag{A68}$$

with the temperature T and the exciton chemical potential μ_{X}. The exciton density is given by $n_{\mathrm{X}} = (1/\mathcal{A}) \sum_{\nu, \mathbf{Q}} N_{\nu, \mathbf{Q}}^{\mathrm{X}}$. According to the bosonic commutator rules, it is

$$i\hbar g^>(\nu_1, \mathbf{Q}_1) = 1 + i\hbar g^<(\nu_1, \mathbf{Q}_1). \tag{A69}$$

In the quasiequilibrium case, evaluating $i\hbar(\partial/\partial t_1) g^{\mathrm{ret}}(\nu_1, \mathbf{Q}_1, t_1)$ with Eqs. (A66) and (A64), an algebraic equation for the retarded exciton Green function can be derived in the frequency domain:

$$\left(\hbar\omega - E_{\nu_1, \mathbf{Q}_1} - \Sigma^{\mathrm{H}}(\nu_1, \mathbf{Q}_1) - \Sigma^{\mathrm{F}}(\nu_1, \mathbf{Q}_1) - \Sigma^{\mathrm{PB}}(\nu_1, \mathbf{Q}_1) - \Sigma^{\mathrm{MW, ret}}(\nu_1, \mathbf{Q}_1, \omega) \right) g^{\mathrm{ret}}(\nu_1, \mathbf{Q}_1, \omega) = 1. \tag{A70}$$

The retarded Green function describes the spectral properties of the dense exciton gas. Many-body interaction effects are taken into account via the self-energy $\Sigma(\omega) = \Sigma^{\mathrm{H}} + \Sigma^{\mathrm{F}} + \Sigma^{\mathrm{PB}} + \Sigma^{\mathrm{MW, ret}}(\omega)$, which acts as a frequency-dependent operator. We introduce a Montroll-Ward self-energy $\Sigma^{\mathrm{MW, ret}}(\omega)$ for excitons, which contains only the retarded part of the GW self-energy (A61). Assuming that excitons can be described as quasiparticles with a renormalized energy $\tilde{E}_{\nu_1, \mathbf{Q}_1}$ and a

broadening $\Gamma_{\nu_1,\mathbf{Q}_1}$, the exciton Montroll-Ward self-energy can be derived along the same lines as in the single-particle case [8,73]:

$$\Sigma^{\text{MW,ret}}(\nu_1, \mathbf{Q}_1, \omega) = i\hbar \sum_{\nu_1', \mathbf{Q}_1'} \int_{-\infty}^{\infty} \frac{d\omega'}{2\pi} \frac{(1 + N_{\nu_1', \mathbf{Q}_1'}^{\text{X}}) \tilde{W}_{\mathbf{Q}_1, \mathbf{Q}_1', \mathbf{Q}_1, \mathbf{Q}_1'}^{>, \nu_1, \nu_1', \nu_1, \nu_1'}(\omega') - N_{\nu_1', \mathbf{Q}_1'}^{\text{X}} \tilde{W}_{\mathbf{Q}_1, \mathbf{Q}_1', \mathbf{Q}_1, \mathbf{Q}_1'}^{<, \nu_1, \nu_1', \nu_1, \nu_1'}(\omega')}{\hbar\omega - \tilde{E}_{\nu_1', \mathbf{Q}_1'} + i\Gamma_{\nu_1', \mathbf{Q}_1'} - \hbar\omega'}. \tag{A71}$$

The plasmon propagators $\tilde{W}^{>/<}(\omega)$ are given by the effective fully screened matrix elements (A62), which are linear combinations of Coulomb matrix elements W in the Bloch basis. Using the unitary transformation to Wannier orbitals as shown in Eq. (A59), the exciton Montroll-Ward self-energy can be expressed in terms of plasmon propagators in the Wannier basis. The latter fulfill the Kubo-Martin-Schwinger relation [73]

$$W_{\alpha\beta,\mathbf{q}}^{>}(\omega) = e^{\hbar\omega/k_B T} W_{\alpha\beta,\mathbf{q}}^{<}(\omega), \tag{A72}$$

which in combination with $2i\text{Im}W_{\alpha\beta,\mathbf{q}}^{\text{ret}}(\omega) = W_{\alpha\beta,\mathbf{q}}^{>}(\omega) - W_{\alpha\beta,\mathbf{q}}^{<}(\omega)$ allows one to directly relate the propagators to the retarded Coulomb interaction:

$$W_{\alpha\beta,\mathbf{q}}^{>}(\omega) = [1 + n_B(\omega)] 2i\text{Im}W_{\alpha\beta,\mathbf{q}}^{\text{ret}}(\omega),$$
$$W_{\alpha\beta,\mathbf{q}}^{<}(\omega) = n_B(\omega) 2i\text{Im}W_{\alpha\beta,\mathbf{q}}^{\text{ret}}(\omega) \tag{A73}$$

with the Bose distribution function $n_B(\omega)$. The retarded fully screened Coulomb matrix is obtained using the inverse dielectric matrix for photoexcited carriers according to Eq. (A60):

$$W_{\alpha\beta,\mathbf{q}}^{\text{ret}}(\omega) = \sum_{\gamma} \varepsilon_{\mathbf{q}}^{-1,\text{ret},\alpha\gamma}(\omega) V_{\mathbf{q}}^{\gamma\beta}. \tag{A74}$$

The dielectric matrix itself is given by

$$\varepsilon_{\mathbf{q}}^{\text{ret},\alpha\beta}(\omega) = \delta_{\alpha,\beta} - \sum_{\gamma} V_{\mathbf{q}}^{\alpha\gamma} \Pi_{\mathbf{q}}^{\text{ret},\gamma\beta}(\omega) \tag{A75}$$

and is discussed in the following subsection.

The instantaneous part of the self-energy is derived from Eqs. (A53), (A55), and (A56) using the approximation for the equal-time (lesser) Green functions (A68) and the splitting of effective matrix elements (A54) into direct and exchange parts:

$$\Sigma^{\text{H}}(\nu_1, \mathbf{Q}_1) = \sum_{\nu_1', \mathbf{Q}_1'} \tilde{V}_{\mathbf{Q}_1, \mathbf{Q}_1', \mathbf{Q}_1', \mathbf{Q}_1}^{\nu_1, \nu_1', \nu_1', \nu_1} N_{\nu_1', \mathbf{Q}_1'}^{\text{X}} = \Sigma^{\text{H,(D)}}(\nu_1, \mathbf{Q}_1) + \Sigma^{\text{H,(X)}}(\nu_1, \mathbf{Q}_1), \tag{A76a}$$

$$\Sigma^{\text{H,(D)}}(\nu_1, \mathbf{Q}_1) = \sum_{\nu_1', \mathbf{Q}_1'} \tilde{V}_{\mathbf{Q}_1, \mathbf{Q}_1', \mathbf{Q}_1', \mathbf{Q}_1}^{(\text{D}), \nu_1, \nu_1', \nu_1', \nu_1} N_{\nu_1', \mathbf{Q}_1'}^{\text{X}}, \tag{A76b}$$

$$\Sigma^{\text{H,(X)}}(\nu_1, \mathbf{Q}_1) = -\sum_{\nu_1', \mathbf{Q}_1'} \tilde{V}_{\mathbf{Q}_1, \mathbf{Q}_1', \mathbf{Q}_1', \mathbf{Q}_1}^{(\text{X}), \nu_1, \nu_1', \nu_1', \nu_1} N_{\nu_1', \mathbf{Q}_1'}^{\text{X}}, \tag{A76c}$$

$$\Sigma^{\text{F}}(\nu_1, \mathbf{Q}_1) = \sum_{\nu_1', \mathbf{Q}_1'} \tilde{V}_{\mathbf{Q}_1, \mathbf{Q}_1', \mathbf{Q}_1, \mathbf{Q}_1'}^{\nu_1, \nu_1', \nu_1, \nu_1'} N_{\nu_1', \mathbf{Q}_1'}^{\text{X}} = \Sigma^{\text{F,(D)}}(\nu_1, \mathbf{Q}_1) + \Sigma^{\text{F,(X)}}(\nu_1, \mathbf{Q}_1), \tag{A77a}$$

$$\Sigma^{\text{F,(D)}}(\nu_1, \mathbf{Q}_1) = \sum_{\nu_1', \mathbf{Q}_1'} \tilde{V}_{\mathbf{Q}_1, \mathbf{Q}_1', \mathbf{Q}_1, \mathbf{Q}_1'}^{(\text{D}), \nu_1, \nu_1', \nu_1, \nu_1'} N_{\nu_1', \mathbf{Q}_1'}^{\text{X}}, \tag{A77b}$$

$$\Sigma^{\text{F,(X)}}(\nu_1, \mathbf{Q}_1) = -\sum_{\nu_1', \mathbf{Q}_1'} \tilde{V}_{\mathbf{Q}_1, \mathbf{Q}_1', \mathbf{Q}_1, \mathbf{Q}_1'}^{(\text{X}), \nu_1, \nu_1', \nu_1, \nu_1'} N_{\nu_1', \mathbf{Q}_1'}^{\text{X}}, \tag{A77c}$$

$$\Sigma^{\text{PB}}(\nu_1, \mathbf{Q}_1) = \sum_{\nu_1', \mathbf{Q}_1'} \left(\tilde{V}_{\mathbf{Q}_1, \mathbf{Q}_1', \mathbf{Q}_1', \mathbf{Q}_1}^{\text{PB}, \nu_1, \nu_1', \nu_1', \nu_1} + \tilde{V}_{\mathbf{Q}_1, \mathbf{Q}_1', \mathbf{Q}_1, \mathbf{Q}_1'}^{\text{PB}, \nu_1, \nu_1', \nu_1, \nu_1'} \right) N_{\nu_1', \mathbf{Q}_1'}^{\text{X}}. \tag{A78}$$

Because of the Coulomb singularity at long wavelength [$\mathbf{Q} = 0$ in Eq. (A54)], the Hartree interaction requires a separate treatment in the Wannier representation. For a charge-neutral system, the macroscopic (leading) term drops out, and only microscopic contributions to Hartree interaction remain. Following the procedure in Ref. [74], we calculate Hartree-type matrix elements by setting the macroscopic eigenvalue of the Coulomb matrix to zero before transforming the matrix

element to the Wannier representation. This means that the dipole-dipole interaction is not screened by the dielectric environment but only by the polarizability of the bilayer itself. This observation is consistent with the model developed in Ref. [18].

The quasiparticle approximation for exciton Green functions implies that the exciton self-energy $\Sigma(\nu_1, \mathbf{Q}_1, \omega) = \Sigma^H(\nu_1, \mathbf{Q}_1) + \Sigma^F(\nu_1, \mathbf{Q}_1) + \Sigma^{PB}(\nu_1, \mathbf{Q}_1) + \Sigma^{MW,ret}(\nu_1, \mathbf{Q}_1, \omega)$ has to be evaluated self-consistently:

$$\tilde{E}_{\nu_1, \mathbf{Q}_1} = E_{\nu_1, \mathbf{Q}_1} + \text{Re}\Sigma(\nu_1, \mathbf{Q}_1, \tilde{E}_{\nu_1, \mathbf{Q}_1}/\hbar),$$
$$\Gamma_{\nu_1, \mathbf{Q}_1} = -\text{Im}\Sigma(\nu_1, \mathbf{Q}_1, \tilde{E}_{\nu_1, \mathbf{Q}_1}/\hbar) + \Gamma_0. \qquad (A79)$$

Since the instantaneous part of the self-energy is real valued, quasiparticle broadening induced by exciton-exciton interaction stems only from the Montroll-Ward self-energy. We additionally introduce a phenomenological broadening Γ_0 that takes into account scattering of excitons with phonons and defects. We choose $\Gamma_0 = 5$ meV independent of the temperature.

Finally, we note that a static limit can be applied to the self-energy similar to the single-particle case [75], which results in a screened-exchange-Coulomb-hole (SXCH) self-energy for excitons:

$$\Sigma^{F,(D)}(\nu_1, \mathbf{Q}_1) + \Sigma^{MW,ret}(\nu_1, \mathbf{Q}_1, \tilde{E}_{\nu_1, \mathbf{Q}_1}/\hbar) \approx \Sigma^{SXCH}(\nu_1, \mathbf{Q}_1)$$
$$= \sum_{\nu_1', \mathbf{Q}_1'} \tilde{W}_{\mathbf{Q}_1, \mathbf{Q}_1', \mathbf{Q}_1, \mathbf{Q}_1'}^{\nu_1, \nu_1', \nu_1, \nu_1'}(\omega = 0) N_{\nu_1', \mathbf{Q}_1'}^X + \frac{1}{2} \sum_{\nu_1', \mathbf{Q}_1'} \left(\tilde{W}_{\mathbf{Q}_1, \mathbf{Q}_1', \mathbf{Q}_1, \mathbf{Q}_1'}^{\nu_1, \nu_1', \nu_1, \nu_1'}(\omega = 0) - \tilde{V}_{\mathbf{Q}_1, \mathbf{Q}_1', \mathbf{Q}_1, \mathbf{Q}_1'}^{(D), \nu_1, \nu_1', \nu_1, \nu_1'} \right). \qquad (A80)$$

From the structure of the exciton Montroll-Ward self-energy, it follows that (static) screening due to photo-excited carriers is applied to the bosonic exchange interaction described by the exciton Fock self-energy. However, the fermionic correction terms to the Fock self-energy are not screened. Also, the exciton Hartree and Pauli-blocking contributions remain unscreened. Besides screening of excitonic exchange, a Coulomb hole self-energy arises and leads to a redshift of energies. Throughout this work, we take into account the full frequency dependence of screening, which is discussed in detail in the following.

5. Excitonic screening in RPA

Consistent with the inverse dielectric function (A25), the dielectric function itself is given by

$$\varepsilon(\mathbf{k} + \mathbf{q}, \mathbf{q}, a, a', \underline{t}_1, \mathbf{k}_2 + \mathbf{q}_2, \mathbf{q}_2, a_2, a_2', \underline{t}_2)$$
$$= \frac{\delta V_{\text{ext}}^{a,a'}(\mathbf{k} + \mathbf{q}, \mathbf{q}, \underline{t}_1)}{\delta V_{\text{eff}}^{a_2, a_2'}(\mathbf{k}_2 + \mathbf{q}_2, \mathbf{q}_2, \underline{t}_2)} \qquad (A81)$$

with the relation between V_{ext} and V_{eff} given in Eq. (A23). Using the definition of the particle-density operator (A9), we obtain

$$\varepsilon(\mathbf{k} + \mathbf{q}, \mathbf{q}, a, a', \underline{t}_1, \mathbf{k}_2 + \mathbf{q}_2, \mathbf{q}_2, a_2, a_2', \underline{t}_2)$$
$$= n_1 \delta_{n_1, n_2} \delta(t_1 - t_2) \delta_{\mathbf{k}, \mathbf{k}_2} \delta_{\mathbf{q}, \mathbf{q}_2} \delta_{a, a_2} \delta_{a', a_2'}$$
$$- \frac{\mathcal{A}}{e} \sum_{\mathbf{k}'} \frac{\delta}{\delta V_{\text{eff}}^{a_2, a_2'}(\mathbf{k}_2 + \mathbf{q}_2, \mathbf{q}_2, \underline{t}_2)} \left\{ \sum_{e, e'} V_{\mathbf{k}, \mathbf{k}', \mathbf{k}'-\mathbf{q}, \mathbf{k}+\mathbf{q}}^{a, e, e', a'} \langle\langle e_{\mathbf{k}'}^\dagger(\underline{t}_1) e'_{\mathbf{k}'-\mathbf{q}}(\underline{t}_1) \rangle\rangle - \sum_{h, h'} V_{\mathbf{k}, \mathbf{k}', \mathbf{k}'-\mathbf{q}, \mathbf{k}+\mathbf{q}}^{a, h, h', a'} \langle\langle h_{\mathbf{k}'}^\dagger(\underline{t}_1) h'_{\mathbf{k}'-\mathbf{q}}(\underline{t}_1) \rangle\rangle \right\}. \qquad (A82)$$

Consistent with the derivation of Hartree-type self-energy terms, we proceed by expanding the single-particle densities in terms of exciton densities according to Eq. (A48) and interpreting the resulting four-particle expectation values as exciton Green functions. This means that Eq. (A82) contains functional derivatives of the exciton Green function with respect to the effective potential, which we have identified before as the polarization function; see Eq. (A28). Thus, the dielectric function has the well-known form $\varepsilon = 1 - V\Pi$ with an excitonic polarization function Π. The polarization function is calculated in RPA by inserting the deltalike vertex function (A32):

$$\Pi(3, 4, \mathbf{k}_2 + \mathbf{q}_2, \mathbf{q}_2, a_2, a_2', \underline{t}_2) \approx \frac{e}{\mathcal{A}} \left\{ \sum_{\mathbf{k}_1, h_1} K(3, a_2, \mathbf{k}_2, h_1, \mathbf{k}_1, \underline{t}_2) K(a_2', \mathbf{k}_2 + \mathbf{q}_2, h_1, \mathbf{k}_1, \underline{t}_2, 4) \right.$$
$$\left. - \sum_{\mathbf{p}_1, e_1} K(3, e_1, \mathbf{p}_1, a_2, \mathbf{k}_2, \underline{t}_2) K(e_1, \mathbf{p}_1, a_2', \mathbf{k}_2 + \mathbf{q}_2, 4) \right\}. \qquad (A83)$$

Since we consider only two-particle Green functions K that describe electron-hole pairs, the band index a_2 has to be an electron index in the first line and a hole index in the second line in Eq. (A83), respectively. We now evaluate Eq. (A82) using the RPA polarization function, introducing the exciton representation (A52) and assuming that Green functions are diagonal in the exciton basis, which results in

$$
\varepsilon(\mathbf{k}+\mathbf{q},\mathbf{q},a,a',\underline{t}_1,\mathbf{k}_2+\mathbf{q}_2,\mathbf{q}_2,a_2,a'_2,\underline{t}_2)
$$

$$
= n_1\delta_{n_1,n_2}\delta(t_1-t_2)\delta_{\mathbf{k},\mathbf{k}_2}\delta_{\mathbf{q},\mathbf{q}_2}\delta_{a,a_2}\delta_{a',a'_2} - i\hbar \sum_{\nu_1,\nu_2,\mathbf{Q}_1,\mathbf{Q}_2} G(\nu_1,\mathbf{Q}_1,\underline{t}_1,\nu_1,\mathbf{Q}_1,\underline{t}_2)G(\nu_2,\mathbf{Q}_2,\underline{t}_2,\nu_2,\mathbf{Q}_2,\underline{t}_1^+)
$$

$$
\times \sum_{\mathbf{k}'}\Bigg\{ \sum_{e,e',h'',\mathbf{k}''} V_{\mathbf{k},\mathbf{k}',\mathbf{k}'-\mathbf{q},\mathbf{k}+\mathbf{q}}^{a,e,e',a'}
$$

$$
\times \Bigg(\sum_{h_1,\mathbf{k}_1}\Phi_{\nu_1,\mathbf{Q}_1}(e',\mathbf{k}'-\mathbf{q},h'',\mathbf{k}'')\Phi_{\nu_1,\mathbf{Q}_1}^*(e''',\mathbf{k}_2,h_1,\mathbf{k}_1)\Phi_{\nu_2,\mathbf{Q}_2}(e'''',\mathbf{k}_2+\mathbf{q}_2,h_1,\mathbf{k}_1)\Phi_{\nu_2,\mathbf{Q}_2}^*(e,\mathbf{k}',h'',\mathbf{k}'')\delta_{a_2,e'''}\delta_{a'_2,e''''}
$$

$$
- \sum_{e_1,\mathbf{p}_1}\Phi_{\nu_1,\mathbf{Q}_1}(e',\mathbf{k}'-\mathbf{q},h'',\mathbf{k}'')\Phi_{\nu_1,\mathbf{Q}_1}^*(e_1,\mathbf{p}_1,h''',\mathbf{k}_2)\Phi_{\nu_2,\mathbf{Q}_2}(e_1,\mathbf{p}_1,h'''',\mathbf{k}_2+\mathbf{q}_2)\Phi_{\nu_2,\mathbf{Q}_2}^*(e,\mathbf{k}',h'',\mathbf{k}'')\delta_{a_2,h'''}\delta_{a'_2,h''''}\Bigg)
$$

$$
- \sum_{h,h',e'',\mathbf{p}''} V_{\mathbf{k},\mathbf{k}',\mathbf{k}'-\mathbf{q},\mathbf{k}+\mathbf{q}}^{a,h,h',a'}
$$

$$
\times \Bigg(\sum_{h_1,\mathbf{k}_1}\Phi_{\nu_1,\mathbf{Q}_1}(e'',\mathbf{p}'',h',\mathbf{k}'-\mathbf{q})\Phi_{\nu_1,\mathbf{Q}_1}^*(e''',\mathbf{k}_2,h_1,\mathbf{k}_1)\Phi_{\nu_2,\mathbf{Q}_2}(e'''',\mathbf{k}_2+\mathbf{q}_2,h_1,\mathbf{k}_1)\Phi_{\nu_2,\mathbf{Q}_2}^*(e'',\mathbf{p}'',h,\mathbf{k}')\delta_{a_2,e'''}\delta_{a'_2,e''''}
$$

$$
- \sum_{e_1,\mathbf{p}_1}\Phi_{\nu_1,\mathbf{Q}_1}(e'',\mathbf{p}'',h',\mathbf{k}'-\mathbf{q})\Phi_{\nu_1,\mathbf{Q}_1}^*(e_1,\mathbf{p}_1,h''',\mathbf{k}_2)\Phi_{\nu_2,\mathbf{Q}_2}(e_1,\mathbf{p}_1,h'''',\mathbf{k}_2+\mathbf{q}_2)\Phi_{\nu_2,\mathbf{Q}_2}^*(e'',\mathbf{p}'',h,\mathbf{k}')\delta_{a_2,h'''}\delta_{a'_2,h''''}\Bigg)\Bigg\}.
$$

$$(A84)$$

Similar to the inverse dielectric matrix (A58), the dielectric matrix elements are identified as

$$
\varepsilon(\mathbf{k}+\mathbf{q},\mathbf{q},a,a',\underline{t}_1,\mathbf{k}_2+\mathbf{q}_2,\mathbf{q}_2,a_2,a'_2,\underline{t}_2) \approx \varepsilon_{\mathbf{k},\mathbf{k}_2+\mathbf{q}_2,\mathbf{k}_2,\mathbf{k}+\mathbf{q}}^{a,a'_2,a_2,a'}(\underline{t}_1,\underline{t}_2)\delta_{\mathbf{q},\mathbf{q}_2}\delta_{\mathbf{k},\mathbf{k}_2}
$$

$$
= \sum_{\alpha,\beta}(c_{\alpha,\mathbf{k}}^a)^*(c_{\beta,\mathbf{k}_2+\mathbf{q}_2}^{a'_2})^* \varepsilon_{-\mathbf{q}}^{\alpha\beta}(\underline{t}_1,\underline{t}_2)c_{\beta,\mathbf{k}_2}^{a_2}c_{\alpha,\mathbf{k}+\mathbf{q}}^{a'}\delta_{\mathbf{q},\mathbf{q}_2}\delta_{\mathbf{k},\mathbf{k}_2}, \quad (A85)
$$

assuming again diagonality in the $\mathbf{k}$ index. We can now expand the Coulomb matrix elements in terms of Wannier functions and make use of the completeness of Bloch states to derive the dielectric matrix in the Wannier representation:

$$
\varepsilon_{-\mathbf{q}}^{\alpha\beta}(\underline{t}_1,\underline{t}_2) = \sum_{a,a',a_2,a'_2} c_{\alpha,\mathbf{k}}^a c_{\beta,\mathbf{k}+\mathbf{q}}^{a'_2} \varepsilon_{\mathbf{k},\mathbf{k}+\mathbf{q},\mathbf{k},\mathbf{k}+\mathbf{q}}^{a,a'_2,a_2,a'}(\underline{t}_1,\underline{t}_2)(c_{\beta,\mathbf{k}}^{a_2})^*(c_{\alpha,\mathbf{k}+\mathbf{q}}^{a'})^*
$$

$$
= n_1\delta_{n_1,n_2}\delta(t_1-t_2)\delta_{\alpha,\beta} - i\hbar \sum_{\nu_1,\nu_2,\mathbf{Q}_1,\mathbf{Q}_2} F(\nu_1,\mathbf{Q}_1,\underline{t}_1,\nu_2,\mathbf{Q}_2,\underline{t}_2)\sum_\delta V_{-\mathbf{q}}^{\alpha\delta}\tilde{\Pi}_{-\mathbf{q}}^{\delta\beta}(\nu_1,\nu_2,\mathbf{Q}_1,\mathbf{Q}_2) \quad (A86)
$$

with

$$
F(\nu_1,\mathbf{Q}_1,\underline{t}_1,\nu_2,\mathbf{Q}_2,\underline{t}_2) = G(\nu_1,\mathbf{Q}_1,\underline{t}_1,\nu_1,\mathbf{Q}_1,\underline{t}_2)G(\nu_2,\mathbf{Q}_2,\underline{t}_2,\nu_2,\mathbf{Q}_2,\underline{t}_1^+). \quad (A87)
$$

Using the momentum conservation implied by the exciton wave functions, the matrix elements of $\tilde{\Pi}$ can be explicitly calculated as

$$
\tilde{\Pi}_{-\mathbf{q}}^{\delta\beta}(\nu_1,\nu_2,\mathbf{Q}_1,\mathbf{Q}_2) = \delta_{\mathbf{Q}_2,\mathbf{Q}_1+\mathbf{q}}M_{\nu_1,\nu_2,\mathbf{Q}_1}^\delta(-\mathbf{q})(M_{\nu_1,\nu_2,\mathbf{Q}_1}^\beta(-\mathbf{q}))^* \quad (A88)
$$

with the wave function overlap

$$M^{\delta}_{\nu_1,\nu_2,\mathbf{Q}_1}(\mathbf{q}) = \sum_{\mathbf{k},e,h}\Phi_{\nu_1,\mathbf{Q}_1}(e,h,\mathbf{k})\left\{\sum_{e'}c^{e'}_{\delta,\mathbf{Q}_1-\mathbf{k}-\mathbf{q}}(c^{e}_{\delta,\mathbf{Q}_1-\mathbf{k}})^*\Phi_{\nu_2,\mathbf{Q}_1-\mathbf{q}}(e',h,\mathbf{k}) - \sum_{h'}c^{h'}_{\delta,\mathbf{k}-\mathbf{q}}(c^{h}_{\delta,\mathbf{k}})^*\Phi_{\nu_2,\mathbf{Q}_1-\mathbf{q}}(e,h',\mathbf{k}-\mathbf{q})\right\}^*.$$

(A89)

Finally, we calculate the retarded dielectric matrix by transforming the Keldysh dielectric matrix (A86) to physical times as discussed in the previous chapter. Assuming stationary exciton distribution functions, one can show that

$$i\hbar F^{\text{ret}}(\nu_1,\mathbf{Q}_1,\nu_2,\mathbf{Q}_2,\omega) = \frac{N^{\text{X}}_{\nu_2,\mathbf{Q}_2} - N^{\text{X}}_{\nu_1,\mathbf{Q}_1}}{E_{\nu_2,\mathbf{Q}_2} - E_{\nu_1,\mathbf{Q}_1} + \hbar\omega + i\gamma}.$$

(A90)

With this, we arrive at the final result [see Eq. (A75)]:

$$\varepsilon^{\text{ret},\alpha\beta}_{\mathbf{q}}(\omega) = \delta_{\alpha,\beta} - \sum_{\delta}V^{\alpha\delta}_{\mathbf{q}}\Pi^{\text{ret},\delta\beta}_{\mathbf{q}}(\omega)$$

(A91)

with the polarization matrix

$$\Pi^{\text{ret},\delta\beta}_{\mathbf{q}}(\omega) = \sum_{\nu_1,\nu_2,\mathbf{Q}_1}\frac{N^{\text{X}}_{\nu_2,\mathbf{Q}_1-\mathbf{q}} - N^{\text{X}}_{\nu_1,\mathbf{Q}_1}}{E_{\nu_2,\mathbf{Q}_1-\mathbf{q}} - E_{\nu_1,\mathbf{Q}_1} + \hbar\omega + i\gamma}M^{\delta}_{\nu_1,\nu_2,\mathbf{Q}_1}(\mathbf{q})(M^{\beta}_{\nu_1,\nu_2,\mathbf{Q}_1}(\mathbf{q}))^*.$$

(A92)

We, thus, derive a microscopic dielectric function that describes excitonic screening in RPA corresponding to the bubble-type polaripzation shown in Fig. 5. Our result is a generalization of the bound-state dielectric function derived by Röpke and Der [76], which has also been used in Ref. [8]. In fact, the Röpke-Der dielectric function can be considered a macroscopic limit of our result. We emphasize that a microscopic treatment of screening encoded in the matrix form of $\varepsilon^{\text{ret},\alpha\beta}_{\mathbf{q}}(\omega)$ is essential to capture local-field effects arising due to the layered structure of the crystal unit cell. The interplay of *interlayer* and *intralayer* interactions in the TMD bilayer is, thereby, naturally taken into account. For numerical calculations,
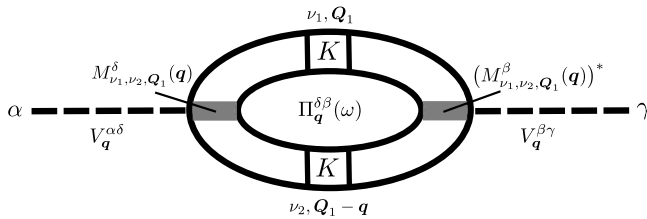

FIG. 5.   Feynman diagram for the excitonic RPA polarization $\Pi^{\delta\beta}_{\mathbf{q}}(\omega)$ inserted between two Coulomb interaction lines in Wannier representation. The interaction vertices depicted in gray correspond to the wave function overlaps defined in Eq. (A89).

we use a phenomenological damping $\gamma = \min(10\text{ meV}, \hbar\omega)$ in Eq. (A92) to ensure the correct analytic behavior in the static limit $\omega \to 0$.

6. Numerical details for the exciton Dyson equation

The exciton energy renormalizations (2) are evaluated self-consistently with the self-energy (3) based on exciton eigenstates from the Bethe-Salpeter equation (BSE) (1). We use a Brillouin zone sampling with $48 \times 48 \times 1$ k points, limiting the Brillouin zone to the regions with radius 2.3 around the K and K' points. The two highest valence and two lowest conduction bands are considered. For every total exciton momentum $\mathbf{Q}$, 48 exciton eigenstates from the BSE are taken into account. Thus, for the given sampling of the Brillouin zone, an energy range between the lowest bound state at about -150 meV and about 100 meV above the continuum edge is covered. This is particularly important to converge the excitonic polarization function that determines the dynamical excitonic screening. Even at elevated densities up to 10^{12} cm^{-2}, only a small fraction of these states is occupied. The larger fraction of unoccupied states is then needed to properly describe the excitonic polarization. The frequency integration in the Montroll-Ward self-energy (A71) extends from -500 to 500 meV using a sampling with 80ω points. We have checked that exciton energy renormalizations are converged to within 1 meV.
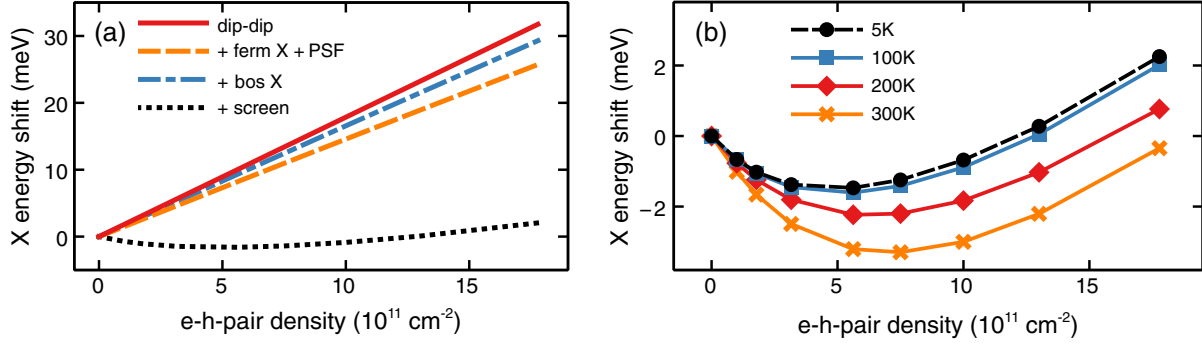
FIG. 6.   Exciton energy renormalizations induced by exciton-exciton interaction. (a) Cumulative density-dependent renormalization of the zero-momentum "gray" $1s$-exciton (spin-triplet) energy at a temperature $T = 100$ K, subsequently adding dipole-dipole interaction (dip-dip), fermionic exchange interaction and phase-space filling (+ ferm X + PSF), bosonic exchange interaction (+ bos X), and screened bosonic exchange (+ screen). The latter represents the result of the full calculation. (b) Calculated temperature and density dependence of energy renormalization for the zero-momentum $1s$-exciton triplet. The result for $T = 5$ K is obtained from extrapolating the high-temperature data.

7. Numerical results for spin-triplet excitons

To complement the numerical results for spin-singlet excitons shown in Fig. 2, we provide data for spin-triplet excitons in Fig. 6. The larger population of triplet states leads to an increase of fermionic and bosonic exchange effects among exciton triplets. As a result, the interaction between exciton triplets is slightly less repulsive than between singlets.

APPENDIX B: EXPERIMENTAL DETAILS

1. Estimation of electron-hole pair density

The injected electron-hole pair density is estimated using the following equation:

$$n_{\mathrm{eh}} = \frac{P\alpha}{f_{\mathrm{rep}}\pi r^2 E_{\mathrm{ph}}} \qquad (B1)$$

with P the laser power (ranging from 250 nW to 25 µW), $\alpha = 0.11$ absorption, $f_{\mathrm{rep}} = 80$ MHz laser repetition rate, $E_{\mathrm{ph}} = 1.63$ eV photon energy (resonant with the MoSe$_2$ $A\!:\!1s$ state), and $r = (0.7 \pm 0.1)$ µm radius of the focused laser spot (according to our previous work [20]). The absorption value is estimated from transfer matrix analysis of reflectance measurements on the heterobilayer; see Fig. 7. For estimating the peak density, the radius is chosen as $r = \mathrm{FWHM}/(2\sqrt{\ln 2})$ so that the effective density is equal to the maximum density of the spot center, $n_{\mathrm{eh}} \times \pi r^2 = N_0$. It is assumed that the majority of the created excitons form interlayer excitons due to the ultrafast charge transfer.

2. Time-dependent energy shifts at higher temperature

A streak camera image acquired at 70 K is presented in Fig. 8(a). It is taken in the spectral region of neutral interlayer triplets, demonstrating the time-dependent change of the emission peak. As the time after the
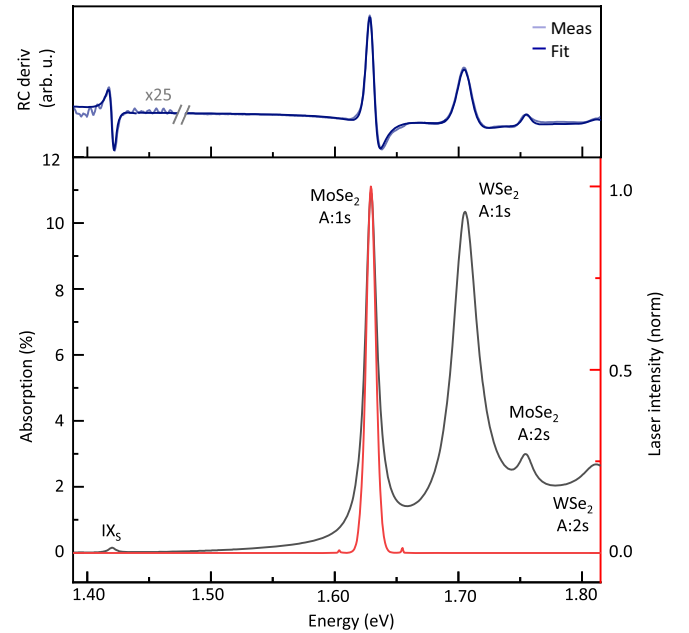

FIG. 7.   (Upper) Reflectance contrast derivative of MoSe$_2$/WSe$_2$ heterobilayer and respective fit from transfer matrix analysis. The extracted parametrized dielectric function is used to obtain the effective absorption spectrum (lower). Spectrum of the pump laser ($\lambda = 761$ nm) in red, overlapping with the absorption peak of the MoSe$_2$ $A\!:\!1s$ state. Adapted from Ref. [20].
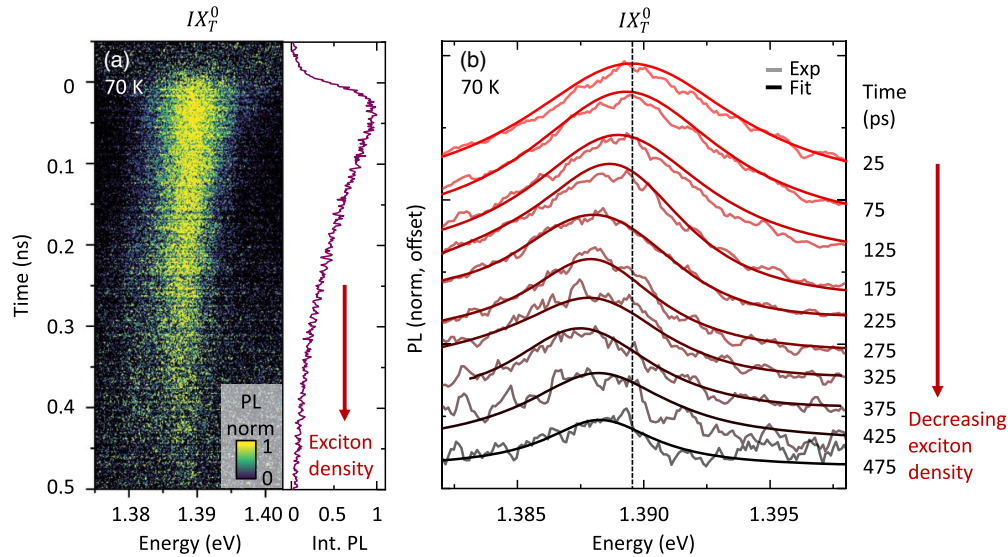
FIG. 8.   Time-dependent energy shift of neutral interlayer triplets at 70 K. (a) Streak camera image of the spectrally and time-resolved PL at a peak density of 10^{12} cm^{-2}. The spectra are normalized at each time step, and the color scale is logarithmic. Corresponding PL transient is presented in the right. (b) Extracted PL spectra at different times after the excitation following the decrease of the PL signal proportional to the exciton density. Included are Gaussian fits, and the dashed line indicates the peak energy immediately after the excitation.

excitation increases, the exciton density and the strength of the PL signal decreases, as illustrated by the transient. For the analysis, we estimate the initial exciton density from the pump fluence and absorption and set the changes of this density proportional to the decrease of the PL signal. Spectra taken at different times are shown in Fig. 8(b) including Gaussian fits to extract peak energies. The data demonstrates the time- and thus density-dependent shift of the emission to lower energies with a weak reversal observable at later times toward higher energies.

[1] H. Fang, C. Battaglia, C. Carraro, S. Nemsak, B. Ozdol, J. S. Kang, H. a. Bechtel, S. B. Desai, F. Kronast, A. a. Unal, G. Conti, C. Conlon, G. K. Palsson, M. C. Martin, A. M. Minor, C. S. Fadley, E. Yablonovitch, R. Maboudian, and A. Javey, *Strong interlayer coupling in van der Waals heterostructures built from single-layer chalcogenides,* Proc. Natl. Acad. Sci. U.S.A. **111,** 6198 (2014).

[2] P. Rivera, J. R. Schaibley, A. M. Jones, J. S. Ross, S. Wu, G. Aivazian, P. Klement, K. Seyler, G. Clark, N. J. Ghimire, J. Yan, D. G. Mandrus, W. Yao, and X. Xu, *Observation of long-lived interlayer excitons in monolayer* $MoSe_2$-WSe_2 *heterostructures,* Nat. Commun. **6,** 6242 (2015).

[3] P. Rivera, H. Yu, K. L. Seyler, N. P. Wilson, W. Yao, and X. Xu, *Interlayer valley excitons in heterobilayers of transition metal dichalcogenides,* Nat. Nanotechnol. **13,** 1004 (2018).

[4] P. Merkl, F. Mooshammer, P. Steinleitner, A. Girnghuber, K.-Q. Lin, P. Nagler, J. Holler, C. Schüller, J. M. Lupton, T. Korn, S. Ovesen, S. Brem, E. Malic, and R. Huber, *Ultrafast transition between exciton phases in van der Waals heterostructures,* Nat. Mater. **18,** 691 (2019).

[5] S. Ovesen, S. Brem, C. Linderälv, M. Kuisma, T. Korn, P. Erhart, M. Selig, and E. Malic, *Interlayer exciton dynamics in van der Waals heterostructures,* Commun. Phys. **2,** 1 (2019).

[6] N. Peimyoo, T. Deilmann, F. Withers, J. Escolar, D. Nutting, T. Taniguchi, K. Watanabe, A. Taghizadeh, M. F. Craciun, K. S. Thygesen, and S. Russo, *Electrical tuning of optically active interlayer excitons in bilayer* MoS_2, Nat. Nanotechnol. **16,** 888 (2021).

[7] E. Barré, O. Karni, E. Liu, A. L. O'Beirne, X. Chen, H. B. Ribeiro, L. Yu, B. Kim, K. Watanabe, T. Taniguchi, K. Barmak, C. H. Lui, S. Refaely-Abramson, F. H. da Jornada, and T. F. Heinz, *Optical absorption of interlayer excitons in transition-metal dichalcogenide heterostructures,* Science **376,** 406 (2022).

[8] A. Steinhoff, M. Florian, M. Rösner, G. Schönhoff, T. O. Wehling, and F. Jahnke, *Exciton fission in monolayer transition metal dichalcogenide semiconductors,* Nat. Commun. **8,** 1166 (2017).

[9] J. Wang, J. Ardelean, Y. Bai, A. Steinhoff, M. Florian, F. Jahnke, X. Xu, M. Kira, J. Hone, and X.-Y. Zhu, *Optical generation of high carrier densities in 2D semiconductor heterobilayers,* Sci. Adv. **5,** eaax0145 (2019).

[10] D. J. Morrow and X. Ma, *Trapping interlayer excitons in van der Waals heterostructures by potential arrays,* Phys. Rev. B **104,** 195302 (2021).

[11] W. Li, X. Lu, S. Dubey, L. Devenica, and A. Srivastava, *Dipolar interactions between localized interlayer excitons in van der Waals heterostructures,* Nat. Mater. **19,** 624 (2020).

[12] E. C. Regan, D. Wang, E. Y. Paik, Y. Zeng, L. Zhang, J. Zhu, A. H. MacDonald, H. Deng, and F. Wang, *Emerging exciton physics in transition metal dichalcogenide heterobilayers,* Nat. Rev. Mater. **7,** 778 (2022).

[13] H. Guo, X. Zhang, and G. Lu, *Tuning moiré excitons in Janus heterobilayers for high-temperature Bose-Einstein condensation,* Sci. Adv. **8,** abp9757 (2022).

[14] X. Sun, Y. Zhu, H. Qin, B. Liu, Y. Tang, T. Lü, S. Rahman, T. Yildirim, and Y. Lu, *Enhanced interactions of interlayer excitons in free-standing heterobilayers*, Nature (London) **610**, 478 (2022).

[15] J. Wang, Q. Shi, E. M. Shih, L. Zhou, W. Wu, Y. Bai, D. Rhodes, K. Barmak, J. Hone, C. R. Dean, and X. Y. Zhu, *Diffusivity reveals three distinct phases of interlayer excitons in* $MoSe_2$/WSe_2 *heterobilayers*, Phys. Rev. Lett. **126**, 106804 (2021).

[16] L. Yuan, B. Zheng, J. Kunstmann, T. Brumme, A. B. Kuc, C. Ma, S. Deng, D. Blach, A. Pan, and L. Huang, *Twist-angle-dependent interlayer exciton diffusion in* WS_2-WSe_2 *heterobilayers*, Nat. Mater. **19**, 617 (2020).

[17] Z. Sun, A. Ciarrocchi, F. Tagarelli, J. F. Gonzalez Marin, K. Watanabe, T. Taniguchi, and A. Kis, *Excitonic transport driven by repulsive dipolar interaction in a van der Waals heterostructure*, Nat. Photonics **16**, 79 (2022).

[18] D. Erkensten, S. Brem, R. Perea-Causín, and E. Malic, *Microscopic origin of anomalous interlayer exciton transport in van der Waals heterostructures*, Phys. Rev. Mater. **6**, 094006 (2022).

[19] J. Choi, J. Embley, D. D. Blach, R. Perea-Causín, D. Erkensten, D. S. Kim, L. Yuan, W. Y. Yoon, T. Taniguchi, K. Watanabe, K. Ueno, E. Tutuc, S. Brem, E. Malic, X. Li, and L. Huang, *Fermi pressure and Coulomb repulsion driven rapid hot plasma expansion in a van der Waals heterostructure*, Nano Lett. **23**, 4399 (2023).

[20] E. Wietek, M. Florian, J. Göser, T. Taniguchi, K. Watanabe, A. Högele, M. M. Glazov, A. Steinhoff, and A. Chernikov, *Nonlinear and negative effective diffusivity of interlayer excitons in moiré-free heterobilayers*, Phys. Rev. Lett. **132**, 016202 (2024).

[21] B. Miller, A. Steinhoff, B. Pano, J. Klein, F. Jahnke, A. Holleitner, and U. Wurstbauer, *Long-lived direct and indirect interlayer excitons in van der Waals heterostructures*, Nano Lett. **17**, 5229 (2017).

[22] P. Nagler, G. Plechinger, M. V. Ballottin, A. Mitioglu, S. Meier, N. Paradiso, C. Strunk, A. Chernikov, P. C. M. Christianen, C. Schüller, and T. Korn, *Interlayer exciton dynamics in a dichalcogenide monolayer heterostructure*, 2D Mater. **4**, 025112 (2017).

[23] W. Li, X. Lu, J. Wu, and A. Srivastava, *Optical control of the valley Zeeman effect through many-exciton interactions*, Nat. Nanotechnol. **16**, 148 (2021).

[24] L. V. Butov, A. Zrenner, G. Abstreiter, G. Böhm, and G. Weimann, *Condensation of indirect excitons in coupled* AlAs/GaAs *quantum wells*, Phys. Rev. Lett. **73**, 304 (1994).

[25] L. V. Butov, C. W. Lai, A. L. Ivanov, A. C. Gossard, and D. S. Chemla, *Towards Bose-Einstein condensation of excitons in potential traps*, Nature (London) **417**, 47 (2002).

[26] A. L. Ivanov, *Quantum diffusion of dipole-oriented indirect excitons in coupled quantum wells*, Europhys. Lett. **59**, 586 (2002).

[27] C. Schindler and R. Zimmermann, *Analysis of the exciton-exciton interaction in semiconductor quantum wells*, Phys. Rev. B **78**, 045313 (2008).

[28] B. Laikhtman and R. Rapaport, *Exciton correlations in coupled quantum wells and their luminescence blue shift*, Phys. Rev. B **80**, 195313 (2009).

[29] S. V. Lobanov, N. A. Gippius, and L. V. Butov, *Theory of condensation of indirect excitons in a trap*, Phys. Rev. B **94**, 245401 (2016).

[30] L. A. Jauregui, A. Y. Joe, K. Pistunova, D. S. Wild, A. A. High, Y. Zhou, G. Scuri, K. De Greve, A. Sushko, C.-H. Yu, T. Taniguchi, K. Watanabe, D. J. Needleman, M. D. Lukin, H. Park, and P. Kim, *Electrical control of interlayer exciton dynamics in atomically thin heterostructures*, Science **366**, 870 (2019).

[31] D. Unuchek, A. Ciarrocchi, A. Avsar, Z. Sun, K. Watanabe, T. Taniguchi, and A. Kis, *Valley-polarized exciton currents in a van der Waals heterostructure*, Nat. Nanotechnol. **14**, 1104 (2019).

[32] Y. E. Lozovik and O. L. Berman, *Phase transitions in a system of two coupled quantum wells*, JETP Lett. **64**, 573 (1996).

[33] L. V. Butov, A. A. Shashkin, V. T. Dolgopolov, K. L. Campman, and A. C. Gossard, *Magneto-optics of the spatially separated electron and hole layers in* GaAs/AlGaAs *coupled quantum wells*, Phys. Rev. B **60**, 8753 (1999).

[34] V. May, F. Boldt, and K. Henneberger, *Many-body theory for the dense exciton gas of direct semiconductors I. General considerations*, Phys. Status Solidi (b) **129**, 717 (1985).

[35] M. Combescot and O. Betbeder-Matibet, *The effective bosonic Hamiltonian for excitons reconsidered*, Europhys. Lett. **58**, 87 (2002).

[36] X. Sun, Y. Zhu, H. Qin, B. Liu, Y. Tang, T. Lü, S. Rahman, T. Yildirim, and Y. Lu, *Enhanced interactions of interlayer excitons in free-standing heterobilayers*, Nature (London) **610**, 478 (2022).

[37] N. Götting, F. Lohof, and C. Gies, *Moiré-Bose-Hubbard model for interlayer excitons in twisted transition metal dichalcogenide heterostructures*, Phys. Rev. B **105**, 165419 (2022).

[38] F. Lohof, J. Michl, A. Steinhoff, B. Han, M. v. Helversen, S. Tongay, K. Watanabe, T. Taniguchi, S. Höfling, S. Reitzenstein, C. Anton-Solanas, C. Gies, and C. Schneider, *Confined-state physics and signs of fermionization of moiré excitons in* WSe_2/$MoSe_2$ *heterobilayers*, 2D Mater. **10**, 034001 (2023).

[39] M. Katzer, M. Selig, L. Sigl, M. Troue, J. Figueiredo, J. Kiemle, F. Sigger, U. Wurstbauer, A. W. Holleitner, and A. Knorr, *Exciton-phonon scattering: Competition between the bosonic and fermionic nature of bound electron-hole pairs*, Phys. Rev. B **108**, L121102 (2023).

[40] F. Boldt, K. Henneberger, and V. May, *Many-body theory for the dense exciton gas of direct semiconductors II. Calculation of exciton level shift and damping in dependence on exciton density*, Phys. Status Solidi (b) **130**, 675 (1985).

[41] H. Haug and S. W. Koch, *Quantum Theory of the Optical and Electronic Properties of Semiconductors*, 5th ed. (World Scientific, Singapore, 2009).

[42] A. Steinhoff, M. Rösner, F. Jahnke, T. O. Wehling, and C. Gies, *Influence of excited carriers on the optical and electronic properties of* MoS_2, Nano Lett. **14**, 3743 (2014).

[43] A. Chernikov, C. Ruppert, H. M. Hill, A. F. Rigosi, and T. F. Heinz, *Population inversion and giant bandgap renormal-*

ization in atomically thin WS$_2$ *layers*, Nat. Photonics **9**, 466 (2015).

[44] S. Ulstrup, A. G. Čabo, J. A. Miwa, J. M. Riley, S. S. Grønborg, J. C. Johannsen, C. Cacho, O. Alexander, R. T. Chapman, E. Springate, M. Bianchi, M. Dendzik, J. V. Lauritsen, P. D. C. King, and P. Hofmann, *Ultrafast band structure control of a two-dimensional heterostructure*, ACS Nano **10**, 6315 (2016).

[45] S. Zhao, Z. Li, X. Huang, A. Rupp, J. Göser, I. A. Vovk, S. Y. Kruchinin, K. Watanabe, T. Taniguchi, I. Bilgin, A. S. Baimuratov, and A. Högele, *Excitons in mesoscopically reconstructed moiré heterostructures*, Nat. Nanotechnol. **18**, 572 (2023).

[46] K. Wagner, J. Zipfel, R. Rosati, E. Wietek, J. D. Ziegler, S. Brem, R. Perea-Causín, T. Taniguchi, K. Watanabe, M. M. Glazov, E. Malic, and A. Chernikov, *Nonclassical exciton diffusion in monolayer* WSe$_2$, Phys. Rev. Lett. **127**, 076801 (2021).

[47] A. Segura, L. Artús, R. Cuscó, T. Taniguchi, G. Cassabois, and B. Gil, *Natural optical anisotropy of h-BN: Highest giant birefringence in a bulk crystal through the mid-infrared to ultraviolet range*, Phys. Rev. Mater. **2**, 024001 (2018).

[48] A. Arora, M. Koperski, K. Nogajewski, J. Marcus, C. Faugeras, and M. Potemski, *Excitonic resonances in thin films of* WSe$_2$: *From monolayer to bulk material*, Nanoscale **7**, 10421 (2015).

[49] M. Selig, G. Berghäuser, A. Raja, P. Nagler, C. Schüller, T. F. Heinz, T. Korn, A. Chernikov, E. Malic, and A. Knorr, *Excitonic linewidth and coherence lifetime in monolayer transition metal dichalcogenides*, Nat. Commun. **7**, 13279 (2016).

[50] F. Cadiz, E. Courtade, C. Robert, G. Wang, Y. Shen, H. Cai, T. Taniguchi, K. Watanabe, H. Carrere, D. Lagarde, M. Manca, T. Amand, P. Renucci, S. Tongay, X. Marie, and B. Urbaszek, *Excitonic linewidth approaching the homogeneous limit in* MoS$_2$-*based van der Waals heterostructures*, Phys. Rev. X **7**, 021026 (2017).

[51] G. Gupta and K. Majumdar, *Fundamental exciton linewidth broadening in monolayer transition metal dichalcogenides*, Phys. Rev. B **99**, 085412 (2019).

[52] Y.-h. Chan, J. B. Haber, M. H. Naik, J. B. Neaton, D. Y. Qiu, F. H. da Jornada, and S. G. Louie, *Exciton lifetime and optical line width profile via exciton-phonon interactions: Theory and first-principles calculations for monolayer* MoS$_2$, Nano Lett. **23**, 3971 (2023).

[53] N. Kumar, Q. Cui, F. Ceballos, D. He, Y. Wang, and H. Zhao, *Exciton-exciton annihilation in* MoSe$_2$ *monolayers*, Phys. Rev. B **89**, 125427 (2014).

[54] S. Mouri, Y. Miyauchi, M. Toh, W. Zhao, G. Eda, and K. Matsuda, *Nonlinear photoluminescence in atomically thin layered* WSe$_2$ *arising from diffusion-assisted exciton-exciton annihilation*, Phys. Rev. B **90**, 155449 (2014).

[55] L. Yuan, T. Wang, T. Zhu, M. Zhou, and L. Huang, *Exciton dynamics, transport, and annihilation in atomically thin two-dimensional semiconductors*, J. Phys. Chem. Lett. **8**, 3371 (2017).

[56] Y. Hoshi, T. Kuroda, M. Okada, R. Moriya, S. Masubuchi, K. Watanabe, T. Taniguchi, R. Kitaura, and T. Machida,

Suppression of exciton-exciton annihilation in tungsten disulfide monolayers encapsulated by hexagonal boron nitrides, Phys. Rev. B **95**, 241403(R) (2017).

[57] A. Raja, L. Waldecker, J. Zipfel, Y. Cho, S. Brem, J. D. Ziegler, M. Kulig, T. Taniguchi, K. Watanabe, E. Malic, T. F. Heinz, T. C. Berkelbach, and A. Chernikov, *Dielectric disorder in two-dimensional materials*, Nat. Nanotechnol. **14**, 832 (2019).

[58] L. Sigl, F. Sigger, F. Kronowetter, J. Kiemle, J. Klein, K. Watanabe, T. Taniguchi, J. J. Finley, U. Wurstbauer, and A. W. Holleitner, *Signatures of a degenerate many-body state of interlayer excitons in a van der Waals heterostack*, Phys. Rev. Res. **2**, 042044(R) (2020).

[59] See Supplemental Material at http://link.aps.org/supplemental/10.1103/PhysRevX.14.031025 for additional data on observations demonstrating the excitation density dependent energy shift of interlayer excitons.

[60] P. Giannozzi *et al.*, QUANTUM ESPRESSO: *A modular and open-source software project for quantum simulations of materials*, J. Phys. Condens. Matter **21**, 395502 (2009).

[61] P. Giannozzi *et al.*, *Advanced capabilities for materials modelling with* QUANTUM ESPRESSO, J. Phys. Condens. Matter **29**, 465901 (2017).

[62] J. P. Perdew, K. Burke, and M. Ernzerhof, *Generalized gradient approximation made simple*, Phys. Rev. Lett. **78**, 1396(E) (1997).

[63] M. J. van Setten, M. Giantomassi, E. Bousquet, M. J. Verstraete, D. R. Hamann, X. Gonze, and G. M. Rignanese, *The PseudoDojo: Training and grading a 85 element optimized norm-conserving pseudopotential table*, Comput. Phys. Commun. **226**, 39 (2018).

[64] R. Gillen and J. Maultzsch, *Interlayer excitons in* MoSe$_2$/WSe$_2$ *heterostructures from first principles*, Phys. Rev. B **97**, 165306 (2018).

[65] S. Grimme, J. Antony, S. Ehrlich, and H. Krieg, *A consistent and accurate ab initio parametrization of density functional dispersion correction (DFT-D) for the 94 elements H-Pu*, J. Chem. Phys. **132**, 154104 (2010).

[66] K. Nakamura, Y. Yoshimoto, Y. Nomura, T. Tadano, M. Kawamura, T. Kosugi, K. Yoshimi, T. Misawa, and Y. Motoyama, *RESPACK: An ab initio tool for derivation of effective low-energy model of material*, Comput. Phys. Commun. **261**, 107781 (2021).

[67] G. Schönhoff, M. Rösner, R. E. Groenewald, S. Haas, and T. O. Wehling, *Interplay of screening and superconductivity in low-dimensional materials*, Phys. Rev. B **94**, 134504 (2016).

[68] C. Steinke, T. O. Wehling, and M. Rösner, *Coulomb-engineered heterojunctions and dynamical screening in transition metal dichalcogenide monolayers*, Phys. Rev. B **102**, 115111 (2020).

[69] M. Rösner, E. Şaşıoğlu, C. Friedrich, S. Blügel, and T. O. Wehling, *Wannier function approach to realistic Coulomb interactions in layered materials and heterostructures*, Phys. Rev. B **92**, 085102 (2015).

[70] M. Florian, M. Hartmann, A. Steinhoff, J. Klein, A. W. Holleitner, J. J. Finley, T. O. Wehling, M. Kaniber, and C. Gies, *The dielectric impact of layer distances on exciton and trion binding energies in van der Waals heterostructures*, Nano Lett. **18**, 2725 (2018).

[71] Z. Gong, G.-B. Liu, H. Yu, D. Xiao, X. Cui, X. Xu, and W. Yao, *Magnetoelectric effects and valley-controlled spin quantum gates in transition metal dichalcogenide bilayers*, Nat. Commun. **4**, 2053 (2013).

[72] F. Katsch, M. Selig, A. Carmele, and A. Knorr, *Theory of exciton-exciton interactions in monolayer transition metal dichalcogenides*, Phys. Status Solidi (b) **255**, 1800185 (2018).

[73] D. Kremp, M. Schlanges, and W.-D. Kraeft, *Quantum Statistics of Nonideal Plasmas* (Springer, Berlin, 2005).

[74] A. Schobert, J. Berges, E. G. C. P. van Loon, M. A. Sentef, S. Brener, M. Rossi, and T. O. Wehling, *Ab initio electron-lattice downfolding: Potential energy landscapes, anharmonicity, and molecular dynamics in charge density wave materials*, SciPost Phys. **16**, 046 (2024).

[75] D. Erben, A. Steinhoff, C. Gies, G. Schönhoff, T. O. Wehling, and F. Jahnke, *Excitation-induced transition to indirect band gaps in atomically thin transition-metal dichalcogenide semiconductors*, Phys. Rev. B **98**, 035434 (2018).

[76] G. Röpke and R. Der, *The influence of two-particle states (excitons) on the dielectric function of the electron-hole plasma*, Phys. Status Solidi (b) **92**, 501 (1979).